NASA/TM-20250009668

Developing the NOAA Next Generation Hyperspectral Microwave Sensor (HyMS): Instrument Concept and Demonstration of Benefits for the NOAA Mission

Antonia Gambacorta
NASA Goddard Space Flight Center, Greenbelt, MD

December 2025

NASA STI Program Report Series

Since its founding, NASA has been dedicated to the advancement of aeronautics and space science. The NASA scientific and technical information (STI) program plays a key part in helping NASA maintain this important role.

The NASA STI program operates under the auspices of the Agency Chief Information Officer. It collects, organizes, provides for archiving, and disseminates NASA's STI. The NASA STI program provides access to the NTRS Registered and its public interface, the NASA Technical Reports Server, thus providing one of the largest collections of aeronautical and space science STI in the world. Results are published in both non-NASA channels and by NASA in the NASA STI Report Series, which includes the following report types:

- **TECHNICAL PUBLICATION.** Reports of completed research or a major significant phase of research that presents the results of NASA Programs and include extensive data or theoretical analysis. Includes compilations of significant scientific and technical data and information deemed to be of continuing reference value. NASA counterpart of peer-reviewed formal professional papers but has less stringent limitations on manuscript length and extent of graphic presentations.

- **TECHNICAL MEMORANDUM**. Scientific and technical findings that are preliminary or of specialized interest, e.g., quick release reports, working papers, and bibliographies that contain minimal annotation. Does not contain extensive analysis.

- **CONTRACTOR REPORT.** Scientific and technical findings by NASA-sponsored contractors and grantees.

- **CONFERENCE PUBLICATION.** Collected papers from scientific and technical conferences, symposia, seminars, or other meetings sponsored or co-sponsored by NASA.

- **SPECIAL PUBLICATION.** Scientific, technical, or historical information from NASA programs, projects, and missions, often concerned with subjects having substantial public interest.

- **TECHNICAL TRANSLATION.** English-language translations of foreign scientific and technical material pertinent to NASA's mission.

Specialized services also include organizing and publishing research results, distributing specialized research announcements and feeds, providing information desk and personal search support, and enabling data exchange services.

For more information about the NASA STI program, see the following:

- Access the NASA STI program home page at http://www.sti.nasa.gov

NASA/TM−20250009668

Developing the NOAA Next Generation Hyperspectral Microwave Sensor (HyMS): Instrument Concept and Demonstration of Benefits for the NOAA Mission

Antonia Gambacorta
NASA Goddard Space Flight Center, Greenbelt, MD

National Aeronautics and Space Administration
Goddard Space Flight Center, Greenbelt, MD

Prepared for NASA Goddard Space Flight Center
under Contract/Task OSAAPIAA 2016-000

December 2025

Available from:

NASA STI Program/Mail Stop 050
NASA Langley Research Center

Hampton, VA 23681-2199

FINAL REPORT

Developing the NOAA Next Generation Hyperspectral Microwave Sensor (HyMS): Instrument Concept and Demonstration of Benefits for the NOAA Mission NOAA Broad Agency Announcement (BAA-NOAA-HyMS-2022)

NAICS code: 541715
GT&C Number: OSAAPIAA 2016-000
Period of Performance: July 1st, 2023 – June 30th, 2025

Antonia Gambacorta[a], Alexander Kotsakis[b], Rachael Kroodsma[a], Matthew Fritts[a], Priscilla Mohammed[c], Joel Johnson[d], Mark Andrews[d], Stephen Nicholls[e], Narges Shahroudi[b], Patrick Stegmann[b], Michael Coon[a], Chase Kielbasa[a], David Robles[a], Sam Weingord[f], Troy Ames[a],Vikram Makrivadr[g], Thomas Mountford[g], Yuchen Zhou[g], Sayed Hashimi[g], Jared Lucey[a], Fabrizio Gambini[h], Victor Torres[a], Shawn Serbin[a], Mark Stephen[a], Jeffrey Piepmeier[a]

Corresponding author: Antonia Gambacorta, antonia.gambacorta@nasa.gov

[a] NASA Goddard Space Flight Center, Greenbelt, MD, USA
[b] Earth System Science Interdisciplinary Center (ESSIC), University of Maryland, College Park, MD, USA
[c] Morgan State University, Baltimore, MD, USA
[d] The Ohio State University, Columbus, OH, USA
[e] SSAI, Inc., Lanham, MD, USA
[f] Newton Engineering, Herndon, VA, USA
[g] Genesis Engineering, Lanham, MD, USA
[h] UMBC/CRESST II, Baltimore, MD, USA

December 2025

Acknowledgment: This project was funded through the Joint Venture Partnerships Program, Office of Systems Architecture and Engineering (SAE), NOAA/NESDIS.

Contents

List of Figures

List of Tables

Executive Summary

This document presents the instrument design, performance analysis and calibration results for the CoSMIR-H (Compact Scanning Microwave Imaging Radiometer - High frequency) instrument following its deployment in the WH^{2}yMSIE field campaign. CoSMIR-H was developed at NASA's Goddard Space Flight Center through the Decadal Survey Incubation (DSI-21) program, representing a significant advancement in hyperspectral microwave sensing technology with over 6,000 channels providing unprecedented vertical resolution for temperature and water vapor retrievals. The WH^{2}yMSIE campaign was designed to ac-quire CoSMIR-H measurements and provide a platform for demonstrating its performance consisting of multiple passive and active sensors, dropsondes and a rich ground network of co-registered in situ measurements. The campaign utilized a comprehensive two-platform airborne approach, deploying the NASA ER-2 high-altitude aircraft and Gulfstream-III with a suite of active and passive remote sensing instruments including advanced radars, lidars, hyperspectral infrared sounders, and CoSMIR-H to synergistically observe atmospheric pro-filing capabilities and advance planetary boundary layer science. The document concludes with recommendations for a hyperspectral microwave space sensor.

This work represents the culmination of a 2-year project aimed at delivering the following milestones: CoSMIR-H instrument design; collection of CoSMIR-H calibrated and quality control data and performance analysis; recommendations for a hyperspectral microwave space sensor.

Key Findings from the project can be summarized as follow.

- **Instrument Performance** CoSMIR-H demonstrated successful operation across multiple frequency bands (50-191 GHz), with comprehensive analysis of brightness temperature (TB) measurements over ocean surfaces. WH^{2}yMSIE ([1]) executed ten high-quality science flights—four over land and six over water—collecting data with more than 60 dropsondes and 27 radiosondes, creating a rich multidimensional dataset for evaluating hyperspectral microwave retrievals. The instrument's hyperspectral capabilities, featuring thousands of channels at high spectral resolution near the 60-GHz oxygen absorption band and 183.3-GHz water vapor line, showed generally good performance characteristics. However, significant 1/f noise was identified in the 183-GHzchannels, which was addressed through a two-step correction process: first smoothing the spectrum over the ASIC chips to eliminate chip-to-chip variations, then apply-ing smoothing filters in the along-scan and along-track directions to remove striping artifacts. Significant scan-dependent biases were discovered and characterized as a function of elevation angle and frequency. The study developed and implemented scan bias corrections, with notably larger corrections required for lower 50-GHz channels compared to higher frequency ranges (175-191 GHz).

- **CoSMIR-H CRTM** A CoSMIR-H CRTM (Community Radiative Transfer Model) coeffcient package was developed to assess observed-minus-calculated (OBS-

CALC) differences using meteorological data from multiple models including HRRR, GEOS-FP, and MERRA-2. The CRTM package was delivered to NOAA as scheduled. During validation work, apparent issues were identified in the CRTM gas absorption model in the oxygen band between 50 and 60 GHz, with discontinuities in vertical optical depth profiles observed around atmospheric model layer 60. This issue was found to affect multiple microwave instruments including ATMS NPP and has been reported to the CRTM core team at the Joint Center for Satellite Data Assimilation for further investigation.

- **Applicability to data assimilation** To address the computational challenges of handling thousands of channels in data assimilation and retrieval applications, a correlation-based channel grouping methodology was developed that reduced the original 2048 channels in the 50 GHz band to 466 grouped channels and 4096 channels in the 183 GHz band to 614 grouped channels, effectively preserving spectral information content while significantly reducing computational requirements and improving noise characteristics.

- **Recommendations for Space** The report concludes with key recommendations for a hyperspectral microwave (HMW) space sensor. Photonic Integrated Circuits (PICs) and Application Specific Integrated Circuits (ASICs) are poised to revolutionize microwave sounding from space, enabling simultaneous, broadband, and hyperspectral measurements of Earth's atmospheric microwave thermal radiation. The Hyperspectral Microwave Photonic Instrument (HyMPI) is first introduced which represents the first laboratory demonstration of PICs applied to hyperspectral microwave sensing. HyMPI pioneers the development of the first space-based HMW sensor: the Advanced Ultra-high Resolution Optical and RAdiofrequency (AURORA) Pathfinder which is also introduced along with a detailed discussion on the state of the art in NEDT and stability defining its technology readiness level. The report concludes with a few notes on future directions undertaken at GSFC to improve CoSMIR-H performance, advance HyMPI and AURORA Pathfinder TRL and perform OSSEs in support of the demonstration of benefits for numerical weather forecast.

- **Publications** Publications and conference proceedings directly and indirectly supported by this grant are summarized in Appendix A.

1. The Conical Scanning Millimeter-wave Imaging Radiometer-Hyperspectral (CoSMIR-H)

1.1. Instrument Description

The Conical Scanning Millimeter-wave Imaging Radiometer – Hyperspectral (CoSMIR-H) was developed at NASA’s Goddard Space Flight Center (GSFC) with funding from NASA’s Earth Science Technology Office (ESTO) through the Decadal Survey Incubation (DSI-21) program. Modified from the well-established CoSMIR sensor, CoSMIR-H is a passive hyperspectral microwave (HMW) sounder that uses new digital spectrometer technology to provide thousands of channels at high spectral resolution near the 60-GHz oxygen absorption band and the water vapor absorption line at 183.3 GHz. CoSMIR-H retained the dual-polarized (vertical and horizontal) window channels at 89 and 165 GHz and replaced the two 50-GHz channels and three 183-GHz channels with hyperspectral channels spanning a range of 8 GHz between 50.0 and 58.0 GHz and a range of 16 GHz between 175.3 and 191.3 GHz. Six Pacific Microchip Corporation (PMCC) third generation (P19800C) Application Specific Integrated Circuit (ASIC) spectrometers give CoSMIR-H 3.906-MHz spectral resolution in these frequency ranges, resulting in 2048 frequencies at 50-58 GHz and 4096 frequencies at 175.3-191.3 GHz. Table 1 gives the CoSMIR-H spectral characteristics and the channel number that corresponds to the order of the channels in the Level 1 files. Note that 89-GHz and 165-GHz channels are not in ascending frequency order but instead are ordered after the hyperspectral channels. The Noise Equivalent Delta Temperature (NEDT) is calculated using in-flight calibration target data (see later section for calculation details).

Table 1: CoSMIR-H SPECTRAL CHARACTERISTICS

Channel Number	Channel	Center Frequency (GHz)	Bandwidth(MHz)	NEDT (K) ☒ = 70 **ms**
1-2048	50-58h	50.002, 50.006, ..., 57.994, 57.998	3.906	1.4
2049-6144	175.3-191.3v	175.302, 175.306, ..., 191.294, 191.298	3.906	3.2

Channel Number	Channel	Center Frequency (GHz)	Bandwidth(MHz)	NEDT (K) ☒ = 70 **ms**
6145-6146	89v/h	89.0±1.25	1500 (x2)	0.2/0.3
6147-6148	165v/h	165.3±1.25	1500 (x2)	0.2/0.2

The DSI-21 program funded the design and development of CoSMIR-H along with engineering check flights in July 2024 on the ER-2. The major modifications to CoSMIR to develop CoSMIR-H included (1) receiver hardware, (2) data system, and (3) ground processing software. CoSMIR-H shares the same mechanical structure as CoSMIR, so all components such as the calibration targets and elevation/azimuth axes remained the same. The 50-GHz and 183-GHz receivers both required additional hardware development to support the wider bandwidths at each channel compared with CoSMIR and to support integration with the ASICs. The data system underwent major upgrades to accommodate the significantly larger data rate and volume. The CoSMIR-H data rate is approximately 3 MB/s compared with the CoSMIR data rate of 1.8 kB/s, giving a total volume close to 80 GB for an 8-hour flight. The raw data collected in-flight is saved at the 3.906-MHz spectral resolution to a disc drive that can be removed from the instrument after flight. The ground processing software was modified to account for the new hyperspectral channels and produces Level 1 NetCDF4 files that contain all 6148 channels.

All the CoSMIR-H receivers and radiometer electronics are housed in a small cylindrical scan head (21.5 cm in diameter and 28 cm in length) that is rotated by a two-axis gimbaled mechanism capable of generating a wide variety of scan profiles. Two calibration targets, one maintained at ambient (cold) temperature of approximately 230-240 K and another heated to a hot temperature of approximately 323 K, are closely coupled to the scan head and rotate with it about the azimuth axis. Radiometric signals from each channel are sampled at 10 ms intervals. These signals and housekeeping data are fed to the main computer in an external electronics box. Figure 1 shows photographs of the CoSMIR-H scan head and scanning pedestal.

Figure 1: Photographs of the CoSMIR-H instrument showing the receivers in the drum (left), the drum closed and the antenna face plate (middle) and the entire instrument on the ground support equipment cart (right).

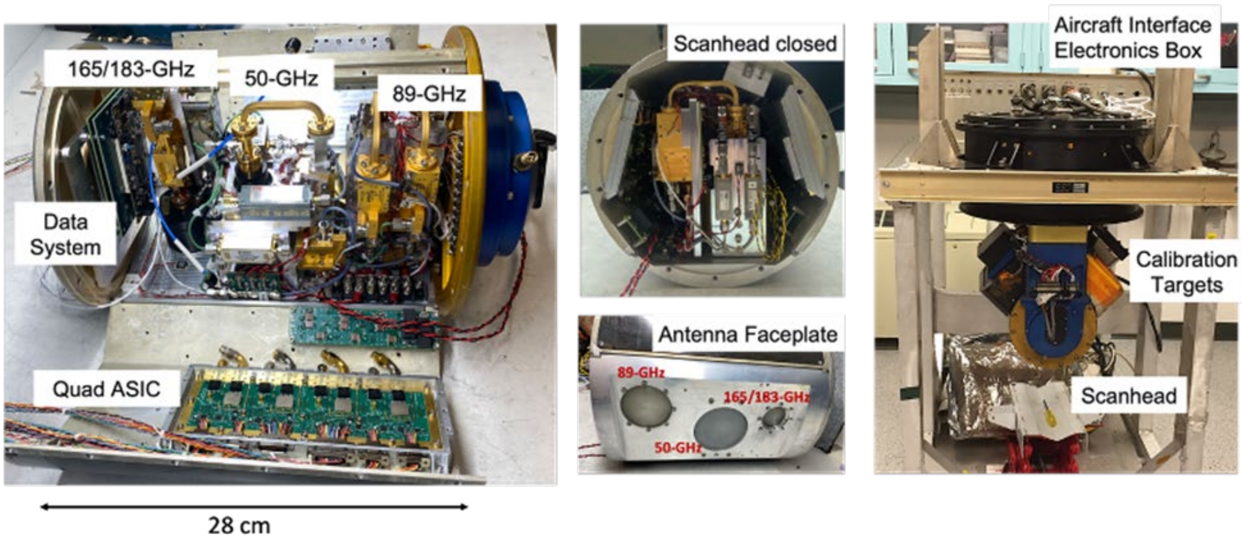

1.2. Scan Geometry

CoSMIR-H's unique scan pedestal can be configured to scan in a variety of pre-programmed profiles. The most common scanning profiles are conical, cross-track, along-track, or a combination of those referred to as a hybrid scan. For the engineering check flights and WH^{2}yMSIE, CoSMIR-H did a cross-track only scan, except for the first WH^{2}yMSIE flight on 10/18 where it did an along-track only scan. In the cross-track only or along-track only configuration, CoSMIR-H views the Earth scene followed by a view of the hot target and then the cold target. The Earth scene was programmed for a 1.5-second scan, with the time to view each calibration target approximately 0.5 seconds. A complete 360 rotation (time between the start of one Earth view scan and the next) takes approximately four seconds. CoSMIR-H was originally programmed to stop and stare at the center of each calibration target to collect sufficient target data (as done by CoSMIR), however, we discovered during the July campaign flights that this resulted in a significant standing wave at the 183-GHz channels. We were able to mitigate this and significantly reduce the standing wave by slowly spinning past the target instead and not using the data from the center of the target. The standing wave section contains a more detailed description on this subject.

CoSMIR-H significantly oversamples in the along-scan direction for observations to be averaged together to help decrease noise. Seven of the 10 ms samples are averaged to give an integration time of 70 ms with a total of 51 samples across the scan for both cross-track and along-track scans. Figure 2 shows the simulated ground track for the resampled 51 scan positions that are given in the Level 1 data files for six adjacent scan lines, assuming an ER-2 ground speed of 200 m/s. The half-power beamwidth is approximately 4.5 for the 50-GHz channels and 4.0 for the 89/165/183 GHz channels.

At an ER-2 cruising altitude of 20 km with 4.0 beamwidth, the nadir effective field of view (EFOV) with 70 ms integration time is 1.4x2.8km and 48 off-nadir EFOV is 2.1x6.4 km.

Figure 2: Simulated ground track scan pattern for CoSMIR for 70 ms integration time for six adjacent cross-track scans. 51 pixels across the scan, -48.2 to +48.2 degrees elevation angle.

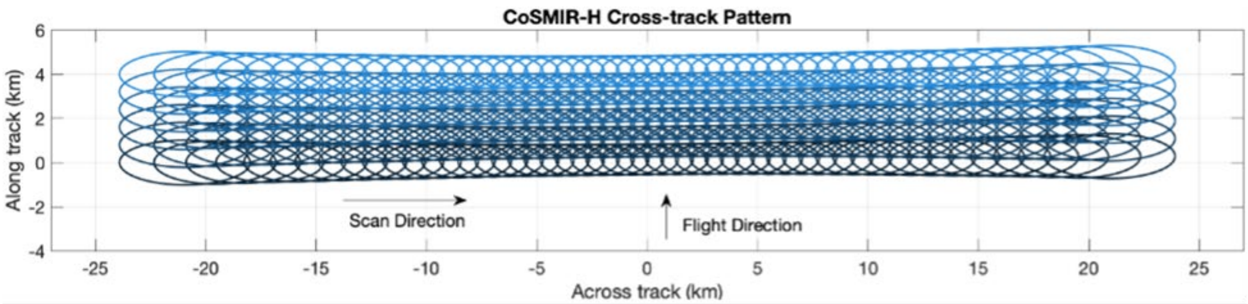

1.3. Calibration Algorithm Overview

The Level 1 product contains calibrated TBs that have been geolocated and quality controlled. The raw Level 0 radiometer voltage counts for each Earth-view pixel across the scan are converted into calibrated TBs using a two-point calibration method that utilizes the onboard hot and cold reference targets between each Earth-view scan. The calibration is extensively analyzed for any anomalies as part of the calibration/validation (cal/val) process. The primary calibration corrections derived from the cal/val analysis were for standing waves, scan biases, and 1/f noise (see Calibration and Validation section for more details on these corrections). There is no antenna pattern correction (APC) applied for CoSMIR-H, as we do not have antenna measurement data. The scan bias correction acts somewhat like an APC to account for edge-of-scan effects and other inconsistencies across the scan. Figure 3 shows a flow chart of the calibration algorithm to go from the Level 0 raw data to Level 1 geolocated and calibrated TBs.

Figure 3: Flow chart for the Level 1 calibration algorithm showing the process for going from Level 0 data to the Level 1 calibrated brightness temperatures.

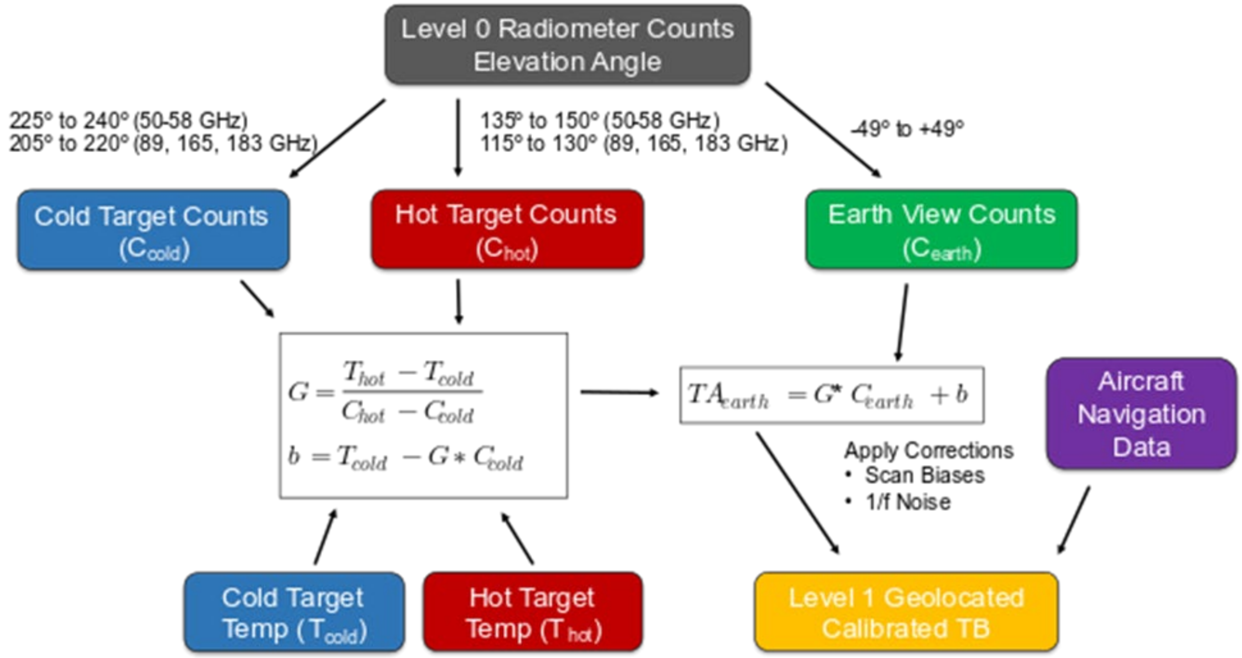

1.4. PMCC ASIC Characteristics and Performance

An in-depth description of the ASICs is given in Baranauskas et al. 2025 and the P19800C data sheet so that will not be repeated here. We will give an overview of specific aspects of the ASIC that affect CoSMIR-H performance and future use of the ASICs in a spaceborne application.

1.4.1. Missing and Low-Quality Data

Certain frequency bins for CoSMIR-H are always set to missing in the Level 1 data files. The missing data are due to the ASIC spurs, which are non-physical spikes in the radiometric data caused by offset, gain, timing, and bandwidth mismatches in the 20 time-interleaved analog-to-digital converter (ADCs) cores located in the front-end ADC. The offset spurs are the largest in magnitude and occur at fractional multiples of the sampling clock, which are consistent among all the ASIC chips. The other spurs are smaller in magnitude and do not appear in all chips, so the CoSMIR-H TB data was extensively analyzed to remove the noticeable spurs. The spur removal results in setting 3 percent of the hyperspectral channels to missing (188 channels set to missing out of 6144 hyperspectral channels). Figure 4 shows an example of how these spurs affect the TB spectrum (left) and the TB spectrum after the spur removal (right). The P19800C data sheet goes into more detail on the spur descriptions and provides information on ways that these spurs can be minimized. In a future spaceborne application that may perform on-orbit bandwidth averaging, these spurs will have to be well-characterized during pre-launch activities to ensure they are removed prior to bandwidth averaging.

Figure 4: Example CoSMIR-H TB spectrum divided into the six ASIC chips showing the magnitude of the ASIC spurs (left) compared with the TB spectrum when the spurs are removed (right). Note that the ASIC bin number does not correspond to increasing frequency for all chips.

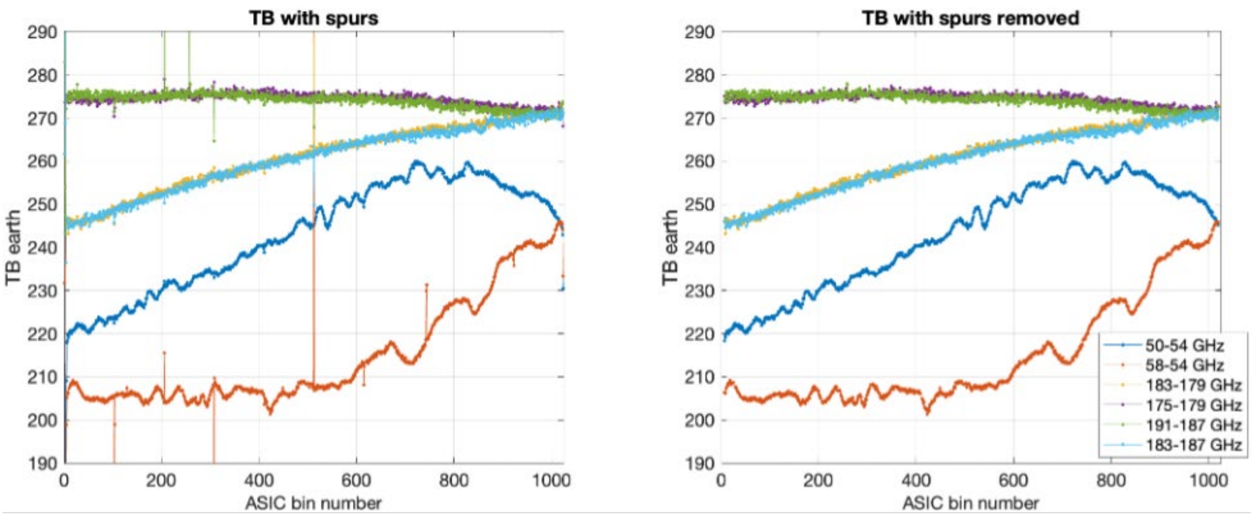

There are also frequency bins that are given a quality flag value of 1, but the TBs are not set to missing. These are frequency bins located within 150 MHz of the edges of the ASIC chips, which is where there is potential fold-over in the radiometric signal from the second Nyquist. These data are only given a warning flag rather than set to missing since the data may be okay to use, but the data user is advised to use with caution.

1.4.2. Power vs Amplitude

The ASIC is configured to obtain the voltage magnitude, however for radiometric measurements the power magnitude is required. To approximate the power magnitude, the radiometric output signal from the ASIC is squared prior to calibrating CoSMIR-H. There is a slight increase to the NEDT of approximately 5 percent by squaring the voltage output vs the ASIC accumulating the power magnitude, which was confirmed with laboratory measurements.

1.4.3. Window Function

A window function is applied to the time-domain signal before a Fast Fourier Transform (FFT) is done to minimize spectral leakage. Various window functions offer different trade-offs between main lobe width (resolution) and side lobe level (leakage), as seen in Figure 5. The window essentially behaves as a filter, with contributions for its estimate over its bandwidth. A measure of this bandwidth is the equivalent noise bandwidth (ENBW) of the window. This is defined as the width of the rectangle filter with the same peak power gain that would accumulate the same noise power. Windows multiply the time series by a tapering function thus data near the edges gets weighted less or zeroed out.

Figure 5: Common window functions that can be used for the ASIC.

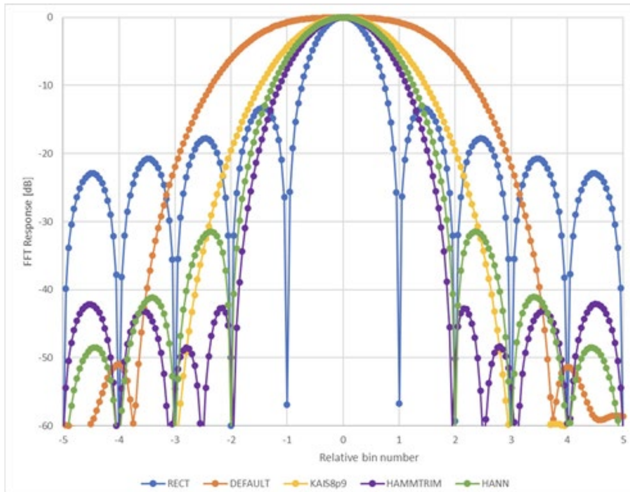

The original window chosen for CoSMIR-H was the default, and the July engineering check flight data were collected with this window setting. After some additional analysis on the window functions, we decided to change this window to something different for WH^{2}yMSIE that would result in a better NEDT for spectral averaging. In an ideal case, the NEDT should drop by a factor of the square root of 1/N where N is the number of frequency bins averaged. However, the windowing leads to correlation between the neighboring frequency bins which results in a higher NEDT than the ideal case when spectral averaging, and the choice of the window will affect how the NEDT drops. See Figure 6 for an example of the NEDT for spectral averaging comparing the default and Hanning windows with the ideal case, which shows that the default window is not a good choice when doing spectral averaging. We decided to choose a window for WH^{2}yMSIE that would result in a spectrally averaged NEDT as close to ideal as possible, so we chose the Tukey window that is a hybrid of the rectangular and Hann windows.

Figure 6: NEDT as a function of spectrally averaged frequency bins, comparing the default and Hanning windows with the ideal NEDT, showing that the default window is not a good choice when averaging frequency bins.

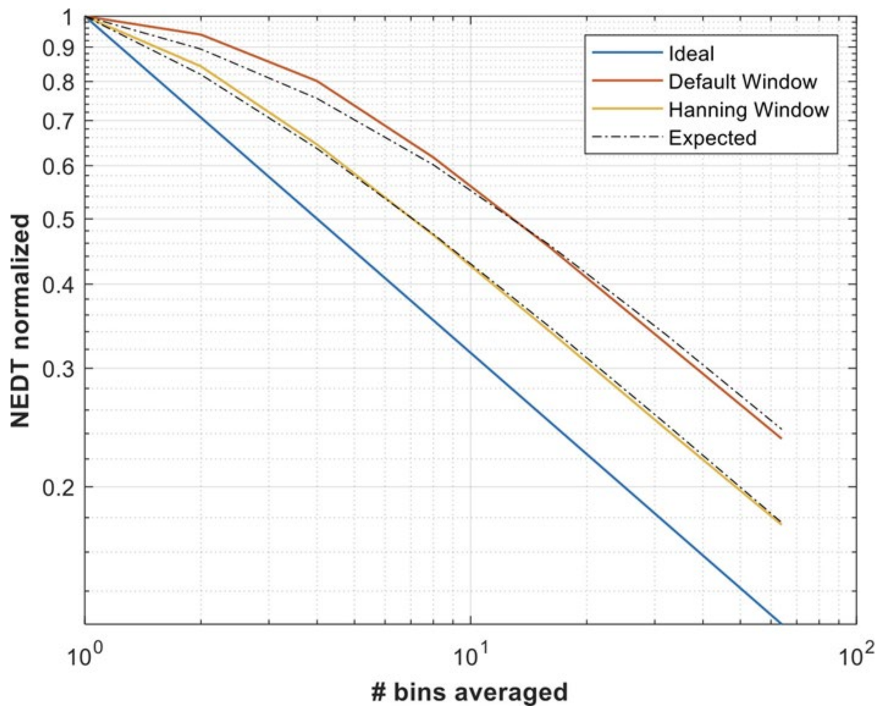

1.4.4. Noise Equivalent Delta Temperature

The NEDT was calculated using laboratory measurements of the receiver noise temperature and was also calculated using in-flight calibration target data. Results are shown in Figure 7 for the 3.906-MHz frequency bins as a function of frequency assuming a 70 ms integration time.

Figure 7: NEDT as a function of frequency for 3.906 MHz bandwidth comparing in-flight with laboratory measurements. The in-flight gives very good agreement with expected values.

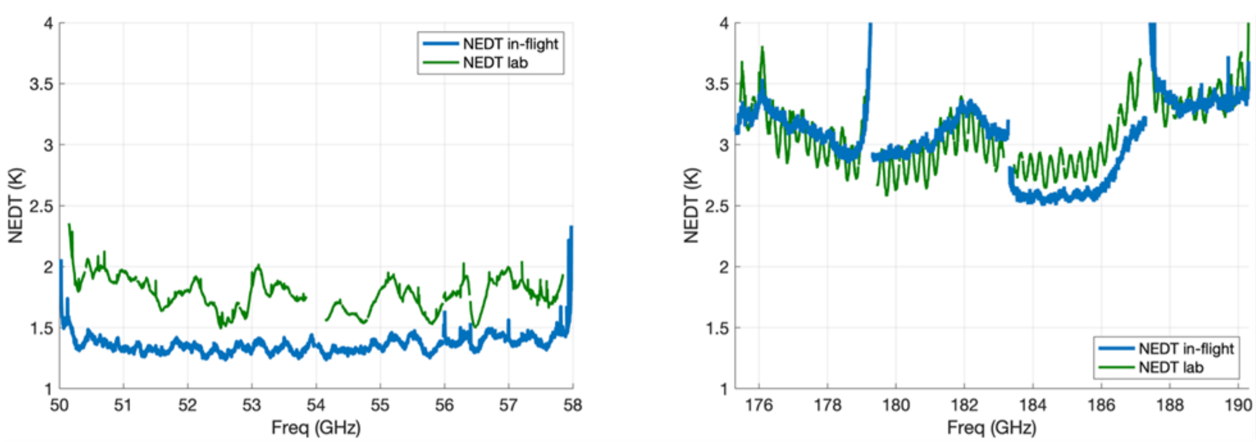

The lab NEDT was calculated from measurements of the receiver noise temperature (TR) pre-flight using the onboard hot target and a liquid nitrogen target. TR varies slightly within each frequency range but is approximately 500 K for the 50-GHz receiver and 1200 K for the 183-GHz receiver. The in-flight NEDT was calculated using the following equation

$$NEDT = \frac{1}{G}\sqrt{\sum_{k=j-n}^{k=j+n} w_{k,j}\overline{C_k^2} - \left(\sum_{k=j-n}^{k=j+n} w_{k,j}\overline{C_k}\right)^2} \qquad (1)$$

where G is the Gain (counts/K), w is the weighting function (taken here to be equal weights), n = 1, j is the scan line number, and Ck is the counts averaged over the samples within a scan line k. The NEDT is calculated as an average over the entire flight after temperatures have stabilized (1 hour into flight). The in-flight NEDT shows very similar or better performance than the laboratory calculations.

There is significant 1/f noise affecting the CoSMIR-H 183-GHz channels (see Calibration and Validation section for a detailed description and correction algorithm). The correction algorithm was developed to adjust the Earth TBs, however, the calibration target counts remained unchanged, therefore it becomes difficult to use the calibration target counts for calculating NEDT as a function of bandwidth averaging.

2. The Westcoast and Heartland Hyperspectral Microwave Sensor Intensive Experiment (WH²yMSIE)

This field campaign originated from our proposal selected from the BAA-NOAA-HyMS-2022 solicitation. This BAA focused on advancing hyperspectral microwave sensing (HyMS) technology through the development and testing of a prototype on airborne or balloon-based platforms. The goal was to assess the value of the collected data and its potential relevance to NOAA's mission with the results helping NOAA evaluate HyMS technology for improved Numerical Weather Prediction (NWP) fore-casts and explore its potential for next-generation space architecture. One year earlier, additional related proposals were selected through the NASA Earth Science Technology Office Instrument Incubator Program (IIP) and Decadal Survey Incubation (DSI) programs in 2021, that supported the development of HyMS sensors and components ([2]. Two of these proposals allowed for the evolution of the CoSMIR instrument to become hyperspectral (CoSMIR-H), enabling the existence of the first airborne hyper-spectral microwave instrument. (WH²yMSIE) started as a technology demonstration, but became a fully integrated field campaign with airborne and ground-based components. The field campaign was conducted in Fall 2024 to demonstrate and evaluate the performance of next-generation hyperspectral microwave remote sensing technology. Through a close partnership, NASA and NOAA, along with numerous academic and research collaborators, led (WH²yMSIE) as a pivotal pathfinder to strengthen future satellite atmospheric profiling capabilities under diverse weather and surface conditions and advance planetary boundary layer (PBL) science [1], [3].

The primary goal of the campaign was to assess the utility of the Hyperspectral Microwave Sensor (HyMS), specifically through demonstration flights of the Conical Scanning Millimeter-wave Imaging Radiometer–Hyperspectral (CoSMIR-H). With more than 100 channels, CoSMIR-H provides an unprecedented level of vertical resolution and sensitivity for temperature and water vapor retrievals. This capability is of particular importance for future satellite missions designed to improve weather forecasting and climate monitoring, especially in challenging cloudy or precipitating conditions where infrared instruments are limited.

2.1. Airborne

WH²yMSIE utilized a two-platform airborne approach, deploying the NASA ER-2 high-altitude aircraft and the Gulfstream-III (G-III) to carry a comprehensive suite of active and passive remote sensing instruments. These included advanced Doppler and cloud radars (MBARS, CRS), lidars (CPL, HALO, AWP), hyperspectral infrared sounders (S-HIS, NAST-I), several microwave and visible/infrared imagers (AMPR, MASTER), and the hyperspectral microwave sounder (CoSMIR-H). The G-III was equipped with dropsondes, which provided the only true validation over ocean for CoSMIR-H retrievals. The payloads were designed to synergistically observe atmospheric thermodynamic structure, cloud microphysics, water vapor distribution, and surface emissivity. All airborne instruments are summarized in Table 2.

Table 2: Table of Instruments, Descriptions and Measurement Information

Instrument	**Description**	**Measurement Type**	**ER2-based Spatial Scale**
Conical Scanning Millimeter-wave Imaging Radiometer - Hyperspectral (CoSMIR-H)	Vertical profiles of temperature, water vapor, and cloud properties	Hyperspectral Microwave	1 km
Microwave Barometric Radar and Sounder (MBARS)	Surface pressure measurements	Doppler Radar	1-4 km
Cloud Radar System (CRS)	High-resolution profiles of reflectivity and Doppler velocity in clouds	Doppler Radar	300 m
Cloud Physics Lidar (CPL)	Cloud optical depth, cloud layer boundaries, and PBL height	Backscatter Lidar	125 m
Scanning-High-resolution Interferometer Sounder (S-HIS)	Vertical profiles of temperature, water vapor	Infrared	2 km
National Airborne Sounder Testbed - Interferometer (NAST-I)	Vertical profiles of temperature, water vapor	Infrared	2.5 km

Instrument	Description	Measurement Type	ER2-based Spatial Scale
Advanced Microwave Precipitation Radiometer (AMPR)	Cloud, precipitation, water vapor, and surface properties (including ocean winds)	Microwave	0.64 km -2.78 km
MODIS-ASTER Airborne Simulator (MASTER)	Cloud properties, aerosol and surface properties	Visible-Infrared	50 m
Airborne Radio Occultation (ARO)	Vertical profiles of temperature and water vapor	GPS Radio Occultation	N/A
High Altitude Lidar Observatory (HALO)*	Vertical profiles of water vapor, aerosol, and cloud optical properties	Differential Absorption Lidar	6-12 km x 315 m
Aerosol Doppler Wind Lidar (AWP)*	Winds from aerosol Doppler shift	Doppler Lidar	2 km
Dropsondes*	Vertical profiles of temperature, water In Situ	In Situ	N/A

2.2. Ground Based Measurements

WH^{2}yMSIE harnessed a number of existing ground-based networks, while also utilizing additional deployable measurements to further enhance the science value of the airborne measurements. Sites that could provide radiosondes were the highest priority, given that these measurements provide the best vertical resolution and serve as the first source of validation for temperature and water vapor retrievals.

The campaign was divided into land and ocean observational phases. Over land, flights targeted a range of surface types—including grasslands, croplands, and arid regions—

aiming to improve surface emissivity models, validate retrievals using collocated radiosonde profiles, and capture diurnal variability in the PBL. Ground-based support was provided by radiosonde launches from NOAA, DOE ARM, NCAR, and CW3E; surface flux and characterization networks such as NEON, AmeriFlux, SURFRAD, and AERONET; and upward-looking sensor platforms like the NSSL CLAMPS, SSEC SPARC, and Vaisala WindCube lidars. Through additional support from NOAA, radiosondes from the National Weather Service (NWS) and dedicated observations from the NSSL CLAMPS trailers, which were equipped with radiosondes, AERI, MWR, and LIDARs were provided specifically for WH^2yMSIE. The U.S. Department of Energy Atmospheric Radiation Measurement (ARM) Southern Great Plains (SGP) observatory's Central Facility (CF) served as an anchor site over land to ensure maximum scientific value for understanding and validating the retrieved temperature and water vapor profiles from the (WH^2yMSIE) instrument payload. The CF site was of prime focus for our overland flights due to the well-observed surface characteristics, wide array of upward remote sensing measurements (e.g. AERI, MWR, Ceilometer), and measurements of skin temperature, which are key to constraining and validating passive retrievals over land surfaces. Through a proposal submitted to DOE ARM, we acquired supplemental radiosonde support (up to 32 RAOBs) from the site and al-lowed for the deployment of the GreenSight WxHive UAS system at the CF site. The radiosonde provided instantaneous profiles coincident with the ER-2 overpass, while the WeatherHive provided a spatial context by measuring T and q profiles in the area around the CF site. Throughout the campaign, there was also coordination with the JPSS team, who have regularly scheduled launches from the ARM SGP site.

Over the ocean, flights were designed to maximize clear-sky underpasses of polar-orbiting reference (POR) satellites, including NOAA-21, EarthCARE, and the Arc-tic Weather Satellite, while also sampling cloudy scenes and complex boundary layer structures such as marine stratocumulus and early-season atmospheric river events. Coordinated flying between the ER-2 and G-III took place primarily over the ocean to take advantage of the highly valuable dropsondes from the G-III. The Catalina Island site also provided valuable observations during a number of over ocean flights by providing occasional radiosondes from CW3E and T/q profiles measurements from GreenSight's WxHive.

In total, the campaign executed ten high-quality science flights—four over land and six over water—collecting data with more than 60 dropsondes and 27 radiosondes. Each flight was strategically planned to underfly key satellite overpasses, span diverse meteorological conditions, and validate observations with robust ground-based and air-borne in situ measurements Table 3. The integration of airborne, surface, and satellite observations created a rich multidimensional dataset for evaluating the performance of hyperspectral microwave retrievals and for developing new algorithms tailored to complex PBL and surface conditions.

WH^2yMSIE represents the first airborne demonstration of hyperspectral microwave technology in this context. Its successful implementation marks a significant milestone in atmospheric remote sensing, providing critical insight into how high-resolution microwave observations can be used for accurate, all-weather retrievals of temperature and moisture profiles. The campaign also highlighted the value of multi-sensor integration for resolving fine-scale processes in the boundary layer, particularly those influencing weather and climate prediction.

2.3. First Look Data Demonstrations

As shown in Figure 9 and Table 3, all of our flights captured a wide variety of environments and surface types. One of the top science goals for WH^{2}yMSIE was to capture as much ocean, clear sky data as possible from CoSMIR-H and under fly program of record (POR) microwave instruments for future inter-comparisons. Clear sky conditions also benefit the infrared sounders, for which we had numerous on the ER-2 aircraft. In Figure 10 are maps of two science flights where ATMS (on NOAA-21) was specifically targeted. The flight plans for the ER-2 were designed to allow CoSMIR-H to be under the NOAA-21 ground track for at least ten minutes before the satellite was overhead to allow for the maximum amount of data points and pixels for future analysis. The flight on October 23, 2024, was the ER-2 aircraft only, while the November 7, 2024, flight also featured the G-III, which provided valuable dropsondes along the satellite ground track.

In addition to taking advantage of clear sky scenes where POR sensors would be overpassing, challenging meteorological conditions were also targeted in an effort to evaluate CoSMIR-H when variable temperature, water vapor, and wind conditions were present. Towards the end of the campaign, we were able to capture an atmospheric river (AR) event, which featured the strongest temperature and water vapor gradients of the campaign. Capturing this dynamic range of conditions is vital for evaluating retrievals in highly variable meteorological conditions. The ER-2 aircraft flew in coordination with the G-III, which provided dropsondes in addition to their remote sensing payload that provided water vapor profiles and 3D winds.

The aircraft performed the first transect across the AR at point "A" (Figure 11, map). CPL and MASTER show how prevalent the cloud cover is within the AR, with multiple cloud levels detected. As the ER-2 flies from "A" to "B", CoSMIR-H captures the decrease in temperature and moisture, the farther north of the AR the aircraft goes. The water vapor profiles from HALO show this decrease in moisture vividly, especially in the free troposphere. As the aircraft continued to "B", they were traveling perpendicular to the strong pressure gradient. This pressure gradient corresponded to strong near surface winds, which was evidenced by the lofting of sea salt aerosol that was captured by CPL. Scattered clouds, including some convective, were detected by using a combination of these three sensors, highlighting the utility of this payload and this rich dataset. The aircraft proceeded to point "C", observing a similar environment compared to what was observed between "A" and "B". This case study, which features a highly impactful AR, serves as a useful case for understanding instrument and retrieval performance under highly dynamic conditions, with varying cloud types.

Figure 8: The WH^{2}yMSIE Logo.

Figure 9: NASA ER-2 (left) and G-III (right) mission flight lines for all flights during WH^{2}yMSIE. Priority ground sites and networks are also plotted on the map

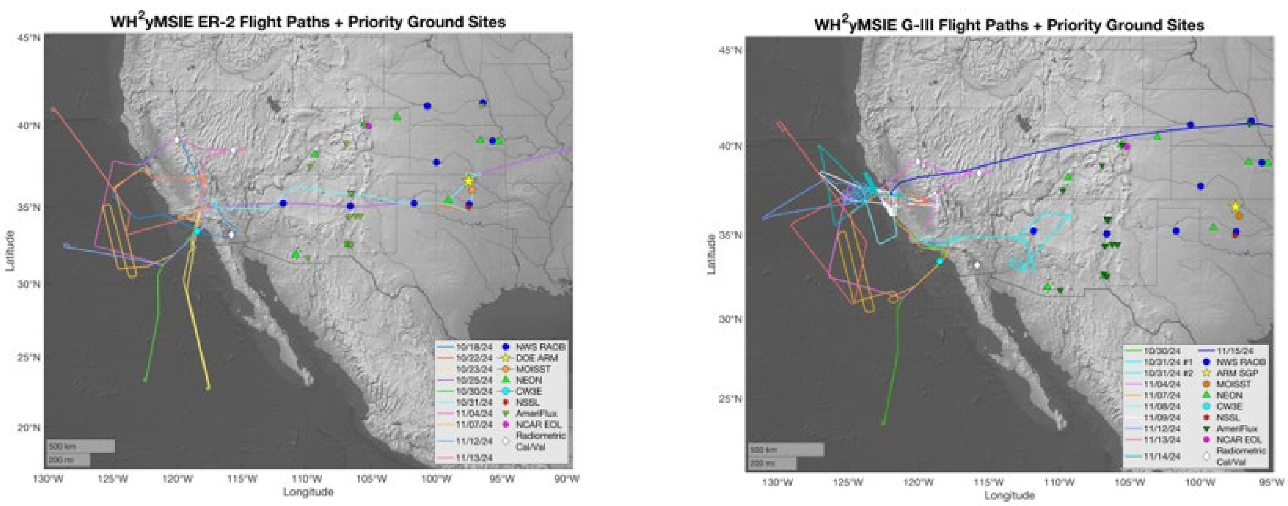

Table 3: Flight Schedule with Ground Targets and Satellite Overpasses.→^{x} denotes the instrument check flight. + denotes coordinated ER-2 flights with the G-III. ⇤ denotes flights that were G-III only.

Flight Date	Focus Area	Ground Site Targets	Satellite Overpasses
October 18, 2024^x	Land	Lake Tahoe, Salton Sea, NOAA Buoys	None

Flight Date	Focus Area	Ground Site Targets	Satellite Overpasses
October 22, 2024	Land	NWS (KFGZ, KABQ, KAMA, KOUN), ARM SGP, NSSL CLAMPS, NEON	NOAA-21
October 23, 2024	Ocean	N/A	NOAA-21, AWS
October 25, 2024	Land	NWS (KFGZ, KABQ, KAMA, KOUN), ARM SGP, NEON, Scott AFB	EarthCare
October 30, 2024+	Ocean	N/A	EarthCare
October 31,2024+	Land	NWS (KFGZ, KABQ, KAMA, KOUN), ARM SGP, NSSL CLAMPS, OSU MOISST, AmeriFlux, NEON, Tuba City (AZ)	None
November 4, 2024+	Land + Ocean	Railroad Valley	AWS
November 7, 2024+	Ocean	Catalina Island (GreenSight, Scripps)	NOAA-21
November 12, 2024	Ocean	Catalina Island (GreenSight, Scripps)	None
November 13, 2024+⇤	Ocean	Catalina Island (GreenSight, Scripps)	EarthCare

Flight Date	Focus Area	Ground Site Targets	Satellite Overpasses
November 15, 2024+⇤	Land	NCAR, NEON, NWS (KOAX),MeadNE (AmeriFlux, Vaisala, SSEC SPARC)	None

Figure 10: ER-2 flight paths from 20241023 and 20241107. The coinciding NOAA-21 ground track (red, dashed line) for those days

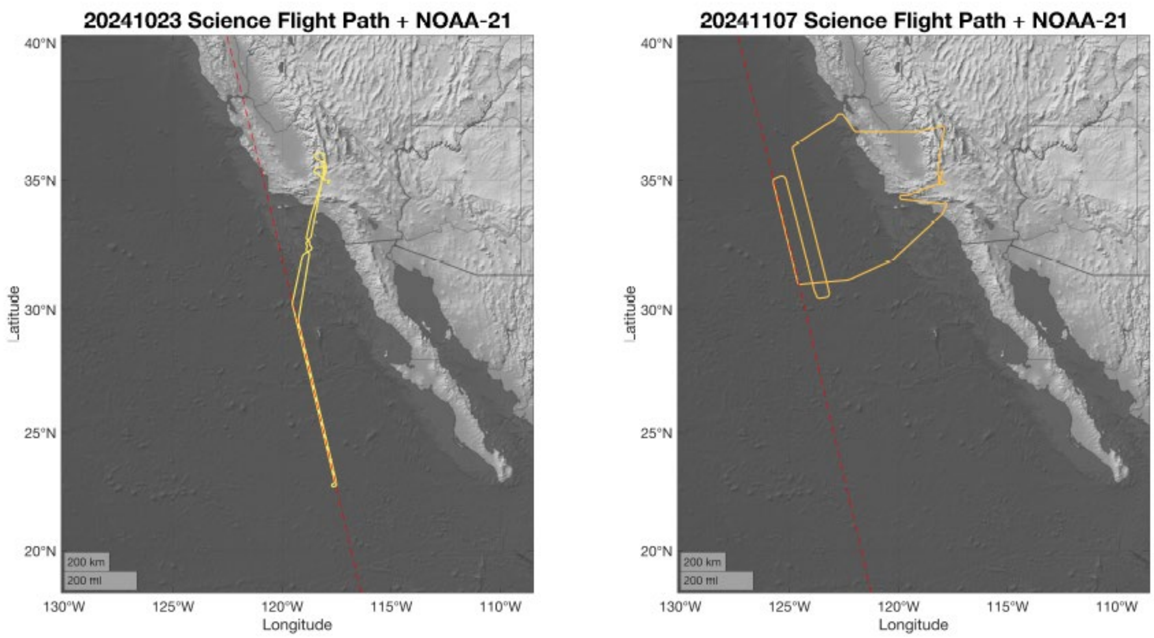

Figure 11: NASA ER-2 and G-III mission flight lines for the flight on November 11, 2024, with forecasted integrated vapor transport (IVT) plotted. Cross section of data from CoSMIR-H (top), CPL (middle), and MASTER (bottom) spanning points A, B, and C.

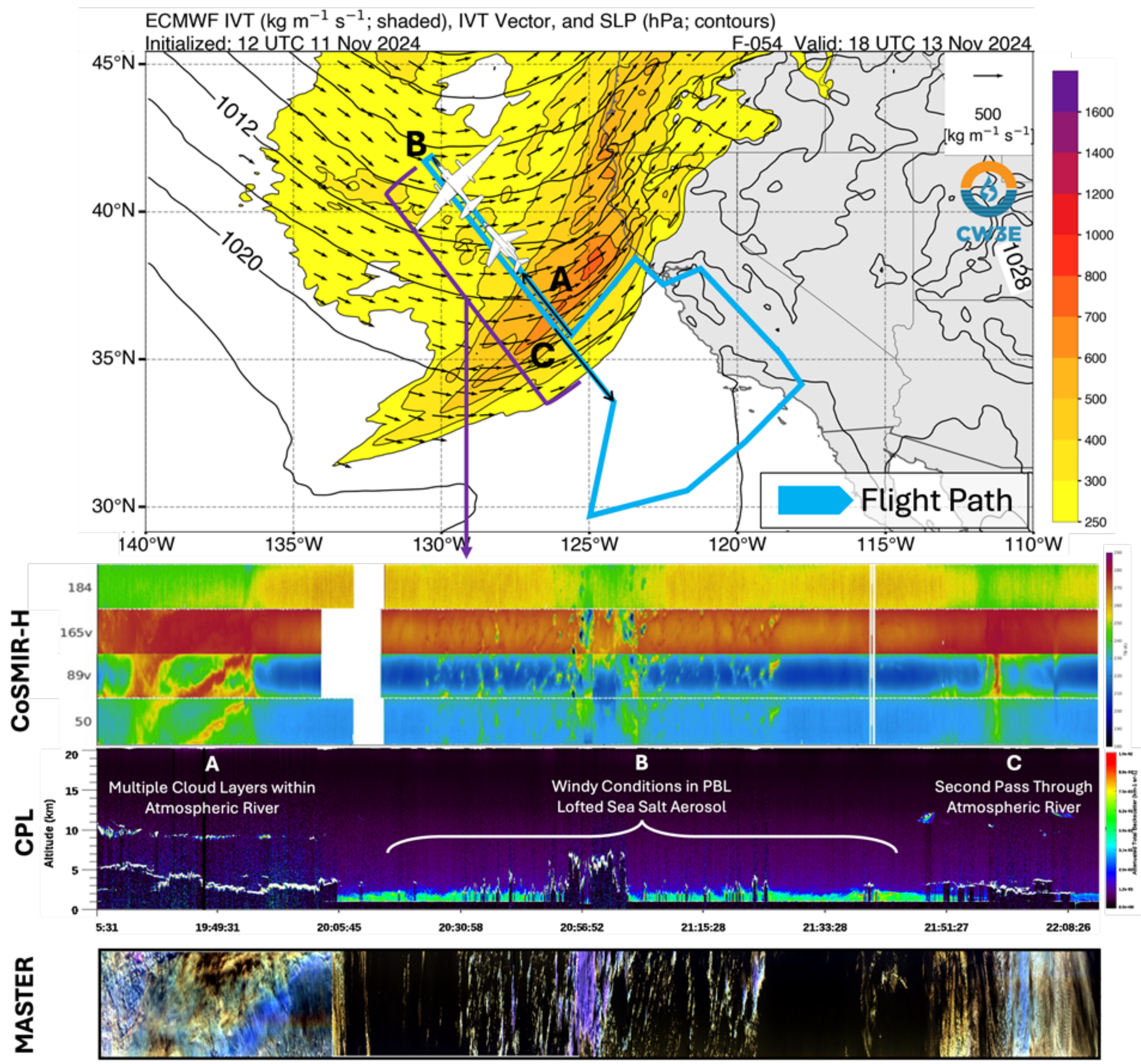

Figure 12: HALO lidar water vapor profiles for the flight through the atmospheric river. Gaps in data (gray) indicates where the lidar could not perform a retrieval due to clouds

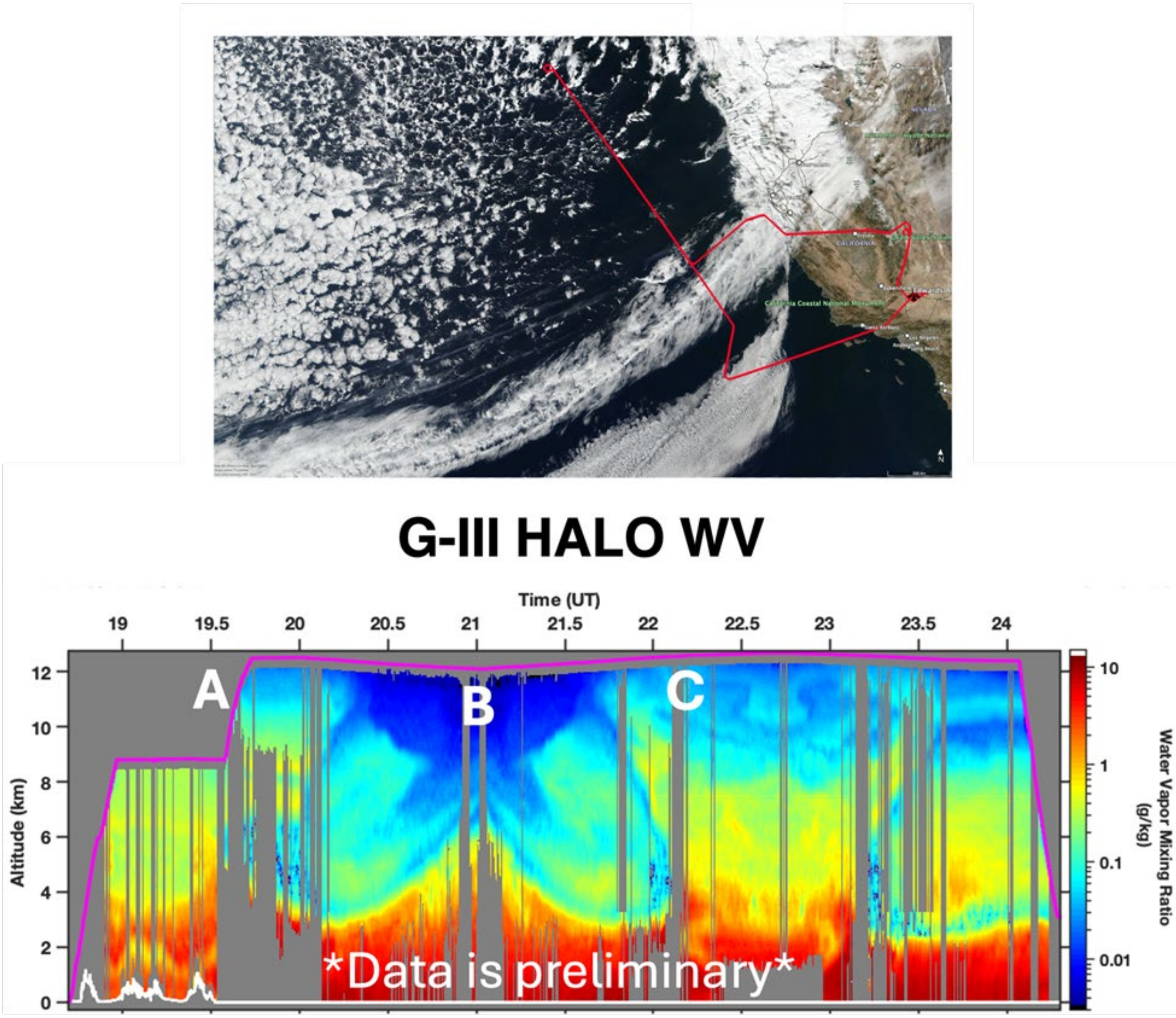

3. Cal/Val Studies

3.1. CoSMIR-H WH^{2}yMSIE Data Overview

The total time of CoSMIR-H observations available from WH^{2}yMSIE is approximately43.5 hours. During normal flight operations, the instrument is turned on just prior to aircraft take-off and turned off during descent, however, the instrument does not start scanning until the ER-2 reaches cruising altitude and stops scanning just prior to de-scent. Therefore, the time of CoSMIR-H data collection is less than the total flight hours. There were also a few issues with the instrument throughout the campaign that caused gaps in the observations, but these were minimal and did not cause significant data loss. The July 2024 engineering check flights campaign collected approximately 20 hours of observations and provided essential information about CoSMIR-H's performance in-flight that allowed the team to optimize the sensor prior to flying again in WH^{2}yMSIE. Due to the experimental nature of these flights and the lower data quality compared to WH^{2}yMSIE, these July flight data are not included in the initial data release.

The Level 1 calibrated brightness temperatures from WH^{2}yMSIE are available to down-load from the LaRC site. There is a data description document that goes into more detail on the data format as well as a description of CoSMIR-H performance for each flight. This document is available here:

https://har.gsfc.nasa.gov/pub/rkroodsm/cosmirh/2024/WH cosmirh_DataUserGuide.pdf.

Quick look images, also known as strip plots, are available to give a quick overview of the CoSMIR-H observations for each flight for a selection of band-averaged channels. These images are given in 1-hour segments as well as for the entire flight. Images from all WH^{2}yMSIE flights can be found here:

https://har.gsfc.nasa.gov/pub/rkroodsm/cosmirh/2024/WHY

As part of the calibration/validation process for CoSMIR-H, the instrument data are extensively analyzed for calibration anomalies. Typical things that are looked at and assessed if corrections are necessary include: geolocation (i.e. instrument pointing), scan biases, gain stability, calibration target anomalies, temperature stability, anomalous data, and absolute calibration. This section includes four calibration/validation items that were assessed and/or corrected: (1) standing waves, (2) 1/f noise, (3) scan biases, and (4) TB comparison with ATMS. Overall, these cal/val analyses show that CoSMIR-H performed extremely well during the campaign and provided quality observations.

3.2. 1/f Noise

Flicker or 1/f noise is a result of receiver gain fluctuations that occur on time scales smaller than the calibration period. This 1/f noise is also referred to as striping due to how it manifests itself in images of the scan data. After collecting data from WH^{2}yMSIE, we noticed significant 1/f noise in the 183-GHz channels that is attributed to the ASIC chips. According to ASIC documentation, gain instability may occur on the order of seconds, however there are some settings in the ASIC variable gain amplifier (VGA) that could improve this. CoSMIR-H performs calibration approximately every four seconds, and it is apparent from the data that the ASIC VGA gain in-stability is a significant problem for CoSMIR-H, primarily for the 183-GHz channels. CoSMIR-H used the default ASIC VGA settings, and we did not experiment with this prior to conducting the airborne flights, so there is potential for improvement to 1/f noise by adjusting these settings. A software correction algorithm was developed to mitigate the 1/f noise in the WH^{2}yMSIE data, and our team has plans to experiment with the ASIC VGA settings to reduce the 1/f noise prior to flying CoSMIR-H again. It is interesting to note that 50-58 GHz channels do not show the same level of 1/f noise as the 183-GHz channels, and there is one chip in the 183-GHz spectrum (183-187 GHz) that has less noise than the other 183-GHz chips.

The algorithm to correct CoSMIR-H 1/f noise is done in two steps. First, discontinuities in the 183-GHz spectrum among the four chips are removed. Since the 50-58 GHz observations did not appear to have significant 1/f noise, those channels do not have a correction applied. Figure 13 (left) shows the 183-GHz spectrum for two different pixels that are in the same scan line approximately 0.5 seconds apart, so both pixels use the same calibration parameters. Colors indicate each ASIC chip to better see the discontinuities. There are jumps in the spectrum between some of the chips, showing that each chip has a different 1/f noise contribution. Analysis of the calibration target data showed that the 183-187 GHz ASIC chip has the least 1/f noise among the four 183-GHz chips. Therefore, for spectrum matching, the 183-187 GHz chip was considered truth, and the other chips were matched to that spectrum to make smooth transitions. As shown in Figure 13, the spectrum matching bias could be different within the same scan line (i.e. the same calibration cycle), so a bias is calculated for each Earth-viewing pixel. The overall curve and pattern of the spectrum for each chip is not changed, there is one bias for each chip applied to all frequencies for that chip on a pixel-to-pixel basis.

Figure 13: Original (left) and corrected (right) TB spectrum at 183-GHz to smooth the spectrum over the ASIC chips for two difference scan pixels (1 and 2) that are approximately 0.5 seconds apart located in the same scan line.

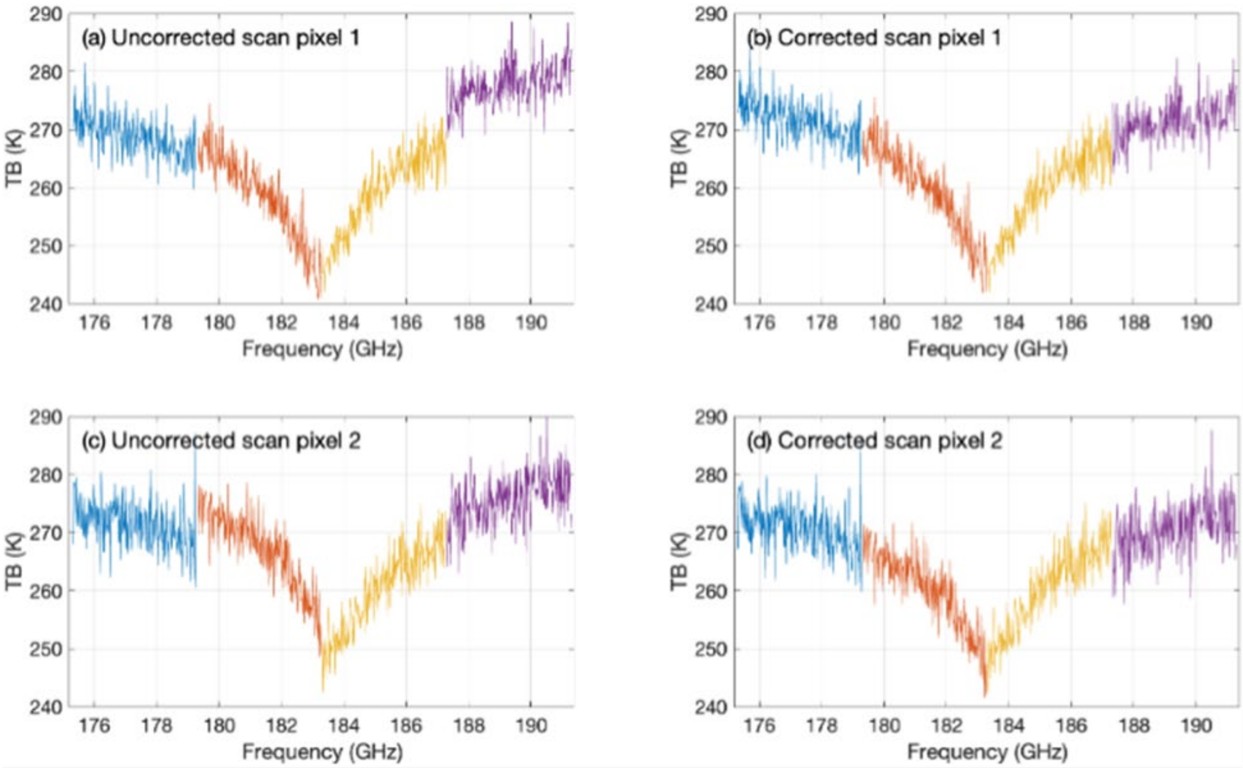

The second step in the 1/f correction smooths the TBs in the along-scan and along-track directions to remove the striping. The first step essentially made all the 183-GHz frequencies have the same 1/f noise as the 183-187 GHz chip. While 183-187 GHz has less 1/f noise, there is still a significant amount of noise in the chip that needs to be removed in the second step. This second step was achieved by applying a smoothing filter to TBs near the water vapor line center and using that as truth to obtain a bias for each pixel, since the TBs at the line center have the least geophysical variability and no sensitivity to the surface. For each pixel, all frequencies are adjusted using the same bias value. Figure 14 shows this striping correction for a 3.906 MHz bandwidth and 4-GHz bandwidth to show how the 1/f noise affects different bandwidths. The thermal noise of individual 3.906-MHz channels is high enough (3 K) to mask some of the 1/f noise, but the striping becomes more apparent when averaging the individual frequency bins into wider bandwidths. This 1/f noise correction algorithm works well for the WH^{2}yMSIE CoSMIR-H data where most of the observations are slow-changing TB scenes. For spaceborne observations in fast-changing TB scenes, a smoothing correction like this may not work as well. A strong 1/f noise correction in software as done here is also not ideal, which is why we plan to experiment with the ASIC settings to reduce the 1/f noise for future CoSMIR-H flights as well as potential spaceborne applications.

Figure 14: Original (left) and corrected (right) TB data at 189.25 GHz for a segment from the 11/13 flight comparing different bandwidths of 3.906 MHz and 4 GHz. The 1/f noise correction significantly reduces the striping.

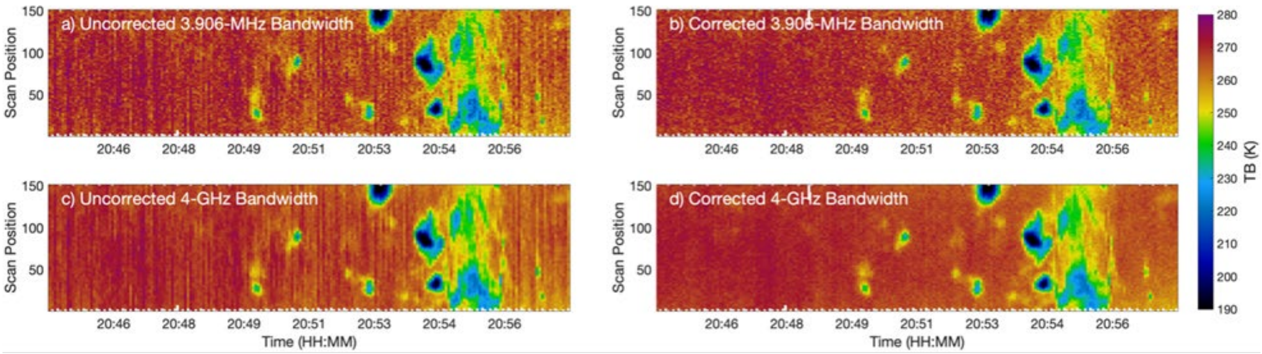

3.3. Scan Bias

CoSMIR-H does not have an antenna pattern correction (APC) applied since we do not currently have measurements of the antenna. Instead, a TB scan bias derived from the observations is applied that acts like an APC to remove some abnormalities and asymmetry seen across the scan. Most of these abnormalities are edge-of-scan effects in the lower 50-GHz channels, which we speculate are either due to some obstruction near the edge of the scan in the main beam or a large sidelobe contributing to the scene TB measured by the antenna. We plan to derive and apply an APC in a future version release.

Figure 15 shows the TB scan bias that is added to the observed TBs as a function of elevation angle (i.e. scan angle) and frequency. Note that the color bar range is significantly different for the two frequency ranges (50-58 and 175-191 GHz). Figure 16 shows the over-ocean TB across the scan for a segment of a flight for one of the lower 50-GHz channels that had a significant correction on the right side of the scan, before (left) and after (right) the scan bias correction.

Figure 15: Bias that is added to the TBs to remove the scan bias. Note the difference in color range for the two frequency ranges showing a significantly

larger correction for some of the lower 50-GHz channels (left: 50-58 GHz, right: 175.3-191.3 GHz).

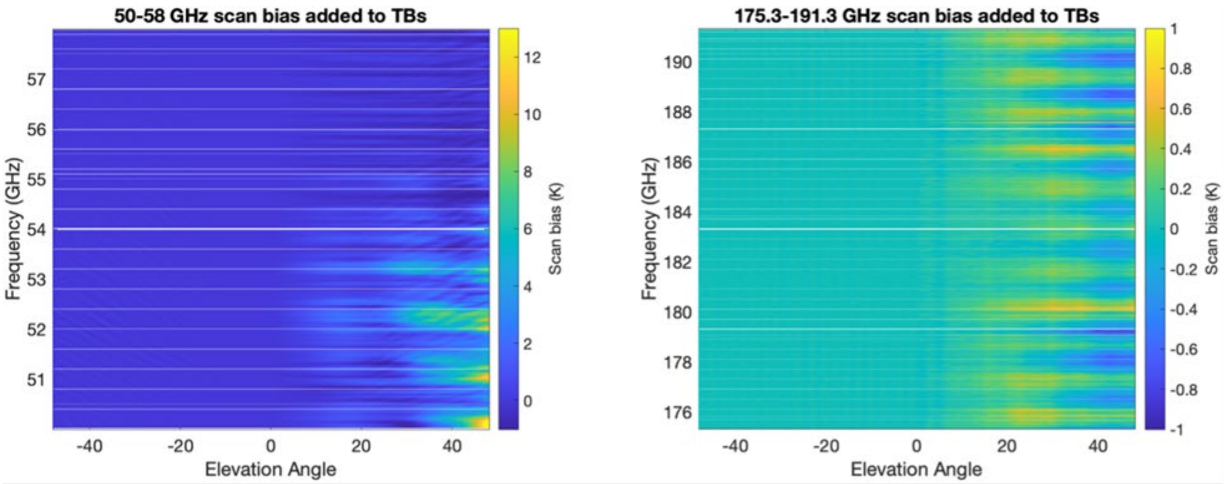

Figure 16: Over-ocean TB for a segment of the 10/23 flight showing the 50.2 GHz TB before (left) and after (right) the scan bias correction. Colored line (blue and green) are individual scans and the black lines are the average.

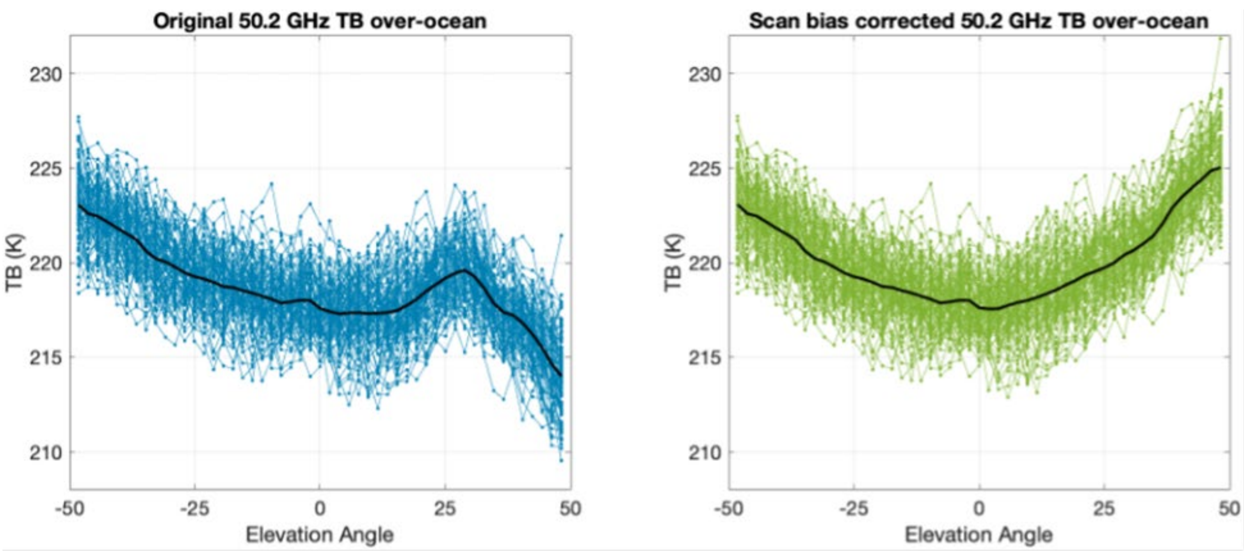

3.4. Comparison with ATMS

We planned and successfully executed two clear-sky over-ocean underflights with the NOAA21 satellite to directly compare CoSMIR-H with the Advanced Technology Microwave Sounder (ATMS) during WH^{2}yMSIE on 10/23 and 11/07. The flight plan consisted of a 30-minute ER-2 flight track close to the satellite ground track with the satellite overhead near the middle of the 30-minute flight track, giving CoSMIR-H observations within 15 minutes of ATMS observations. The footprints differ significantly (CoSMIR-H 1.5 km at nadir compared with ATMS 183-GHz 15 km at nadir), but the clear-sky over-ocean gives a homogeneous scene to better allow direct brightness temperature comparisons.

Figure 17 shows a comparison between CoSMIR-H and ATMS for selected channels. The CoSMIR-H hyperspectral channels are averaged into ATMS-like bandwidths using the NOAA21 ATMS spectral response functions. This comparison shows extremely good agreement between the two sensors for the 89, 165, and 183 GHz channels but does have some significant differences for the lower 50-GHz channels (3-5 K). This may be due to spatial resolution differences, but we speculate this could also be due to the lack of a proper antenna pattern correction at those frequencies, which we will explore in future analysis. The 54.94 and 55.5 GHz channel differences are mostly attributed to the atmospheric contribution above 20 km that the ER-2 does not see but is seen by ATMS.

Figure 17: CoSMIR-H TB comparison with ATMS during two overpass flight legs, plotted as a function of latitude with the two overpasses separated by the dashed line. Black lines are ATMS observations, blue lines are CoSMIR-H observations.

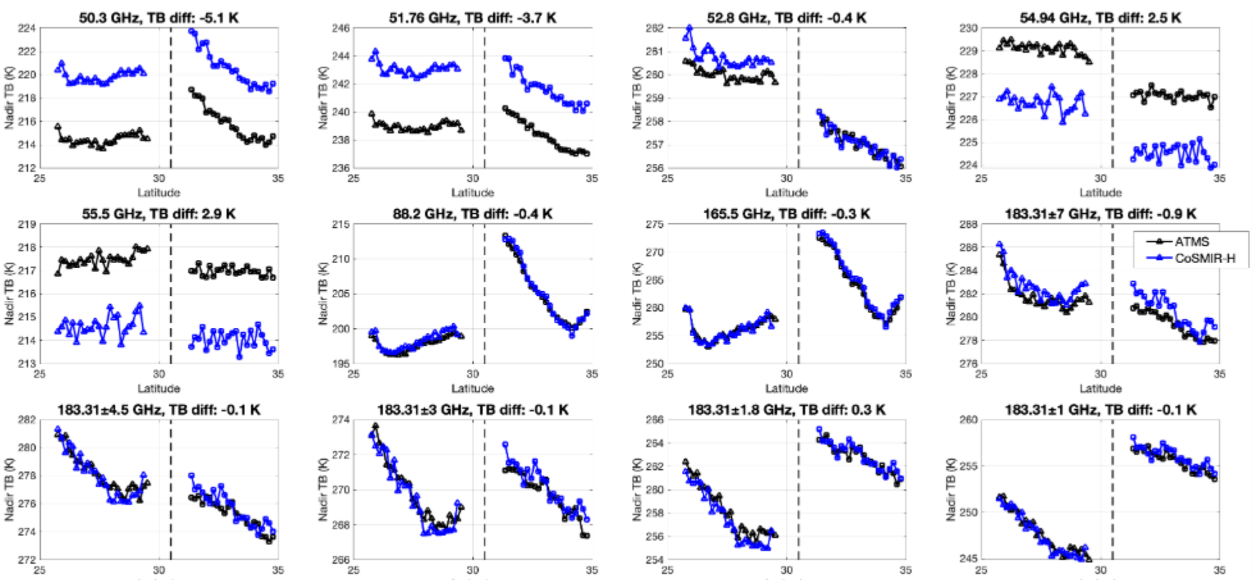

3.5. Analysis of CoSMIR-H Standing Wave Effects

3.5.1. Standing Wave Behavior

As discussed previously, CoSMIR-H calibration uses data from internal “hot” and “cold” targets that are observed during each scan. Early test flights used data in which the scan head “stared” at a fixed hot or cold target scan angle to acquire calibration data. This process resulted in brightness temperatures that showed an oscillatory pattern versus frequency as shown in Figure 18. These non-physical “standing wave” behaviors are caused by interference among reflections within the instrument and/or from the calibration targets. Subsequent test flights eliminated the staring process and maintained a continuous scan over the calibration targets. This allowed data to be examined post-flight to determine angle ranges that reduced standing wave effects. Using this process, desirable angles were identified by GSFC and used in the delivery of CoSMIR-H products for science analysis. To better characterize standing wave behaviors, a fast Fourier transform (FFT) was performed on the brightness temperature versus frequency data within a specified set of scan head angles. Any oscillatory behaviors versus frequency should then appear as large amplitudes in the FFT outputs; the FFT ‘bins’ of the out-put have values defined as cycles per GHz, or seconds. Using the cycles per GHz of the maximum, an approximate distance to an apparent reflection can be ascertained under the assumption of free space propagation. Any non-uniformities in the environment at this distance can help to interpret the reflection source observed.

Figure 18: Standing waves in 175-177.5 GHz data when viewing a particular scan angle

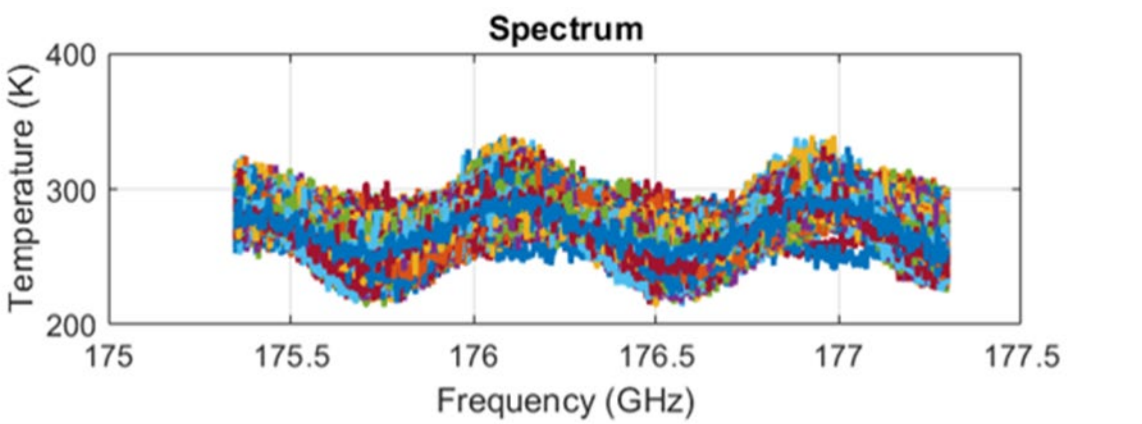

From the FFT data collection, the amplitudes at particular cycles per GHz for each scan angle were calculated and then averaged over a range of scans considered. This average was then plotted with respect to the scan angle (see example in Figure 19). Large amplitudes at 1.024 and 1.536 cycles/GHz occur in the center of each of the calibration targets, as well as in the areas between the targets.

Figure 19: Average standing wave amplitude over the entire travel of a scan for varying cycles/GHz values; angles corresponding to the hot and cold calibration targets and Earth scene indicated by shading

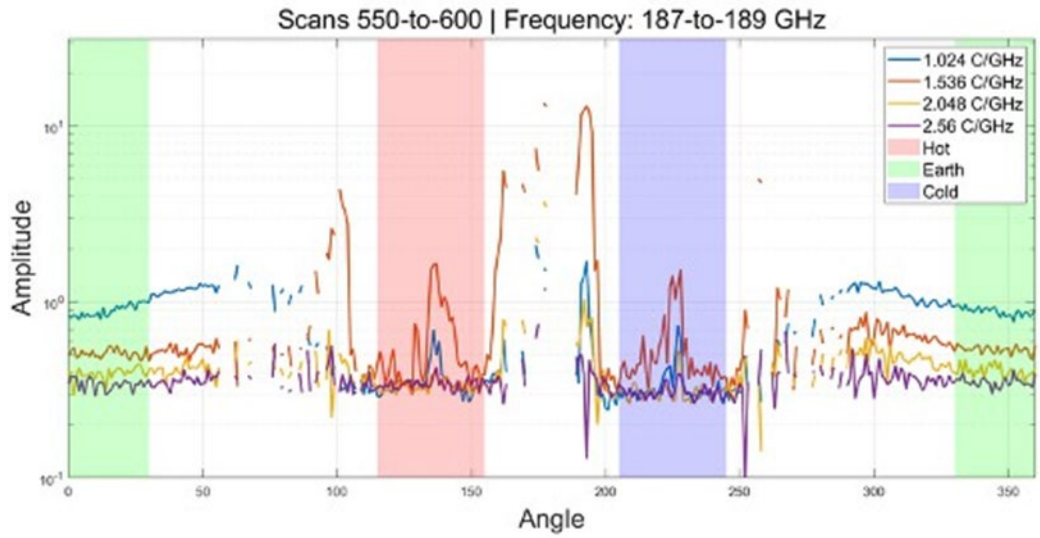

The calibration process was next examined as the angle range used for each of the calibration targets was varied. Here we consider "low-angle", "central-angle", and "high-angle" subsets, as well as an “all-angle” set. Because the hot target occupies 115°-to-155° and the cold target occupies 205°-to-245°, the low and high angle subsets consist of the first and the last fifteen-degree segment of each target, respectively (see Figure 20). The central angle subset, wherein the largest standing wave appears, consists of the ten degrees between the two other subsets. The COSMIR-H baseline calibration at frequencies greater than 100 GHz uses the low-angle subset, which may also be impacted by the physical location of the antenna at this frequency, being biased toward the lower angles of each target.

Figure 20: Standing wave amplitude over the span of the hot and cold targets, with “low”, “center”, and “high” angle regions shaded

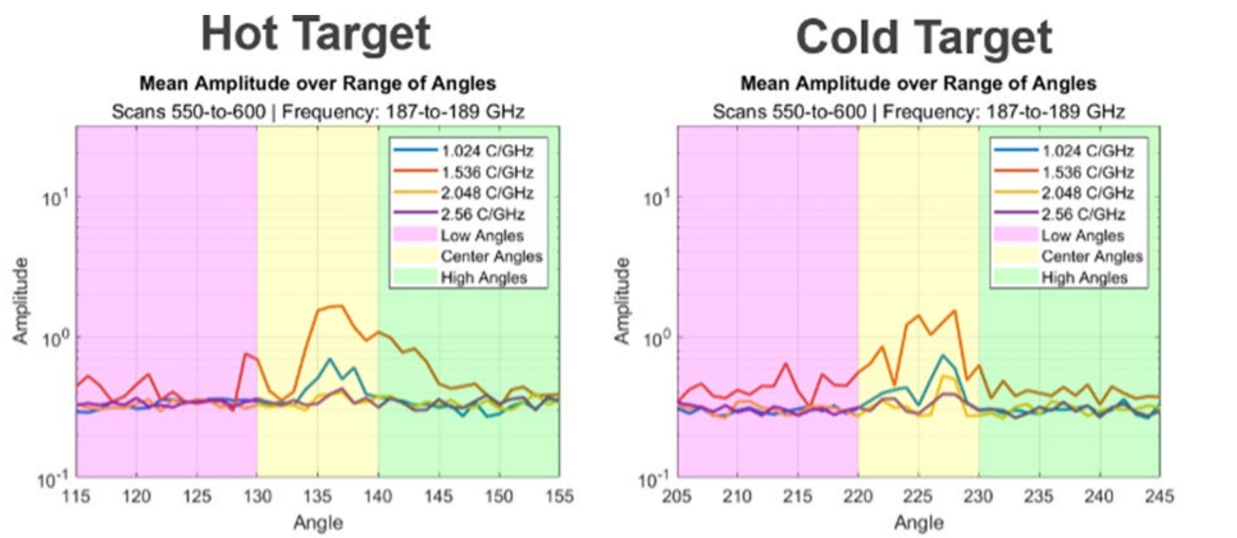

Figure 21 compares calibrated Earth scene brightness temperatures near 187 GHz for the differing calibration target subsets, as well as the change from the baseline “low angles” case. Overall biases shown are less than 1 K, and show some evidence of residual standing wave effects that are greatly reduced compared to those seen on the calibration targets themselves. Given the reduced evidence of standing waves in the “low angle” subset (Figure 3), it should be expected that residual standing wave contributions are even smaller in this range. These results suggest the baseline calibration approach used for science analysis should have only minimal standing wave contributions. The presence of standing wave effects in general, however, motivates careful design of future wideband systems to ensure that potential reflection effects are well described and compensated in the calibration process.

Figure 21: Comparison of Earth brightness temperatures using differing calibration target angle subsets (left) Brightness temperature values (right) Difference from baseline

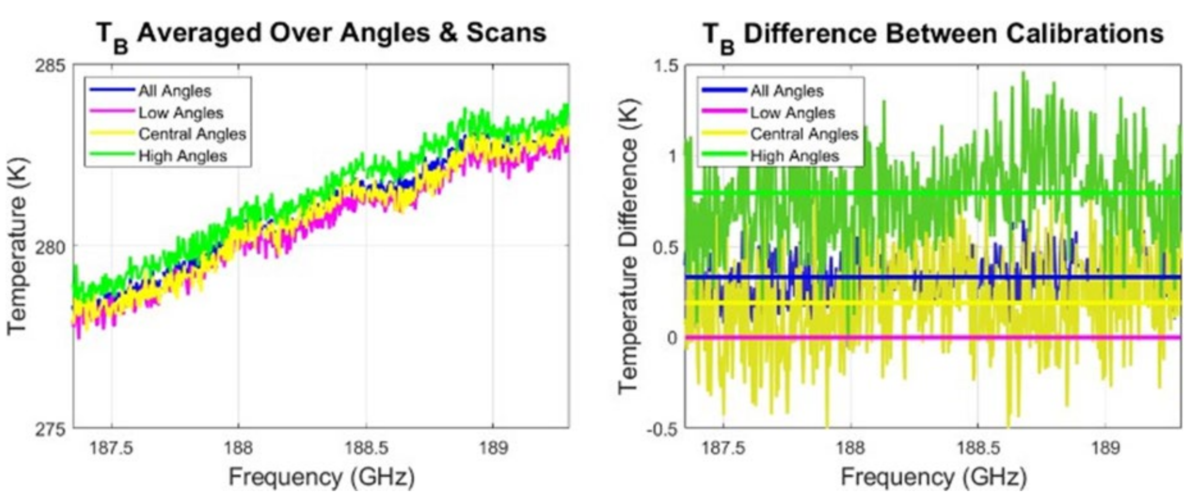

3.5.2. Noise wave modeling of HyMPI Standing Wave effects

Overview of Calibration Process: As seen above, the standard calibration process for radiometers is to observe two targets at known temperatures and develop calibration curves from those observations. One target is the “hot” target - typically at room temperature or higher – and the other target is the “cold” target, typically cooled to a temperature below the instrument temperature. A linear fit calibration curve (“cal curve”) models the received power versus the target temperature. This cal curve can then take any received power and convert it to an observed brightness temperature.

During the course of the project, the HyMPI instrument underwent calibration testing in a lab setting where the hot target was an absorber material at room temperature and the cold target was an open dewar of boiling liquid nitrogen. These targets have different reflection coefficients (affecting the thermal emission from the target) and were at different distances from the instrument. Using a “noise-wave” model developed for analyzing wideband radiometer calibration effects, including the impacts of phase in reflections, we simulated whether the change in target distance influenced the calibration process by introducing standing waves that impact recorded power.

Noise wave model inputs: A block diagram of the HyMPI radiometer is provided in Figure 22. Due to limited information available and the expected impact of downstream components, the noise-wave simulation only includes the antenna, the first LNA, and the high-pass filter.

Figure 22: Block Diagram of HyMPI radiometer front end

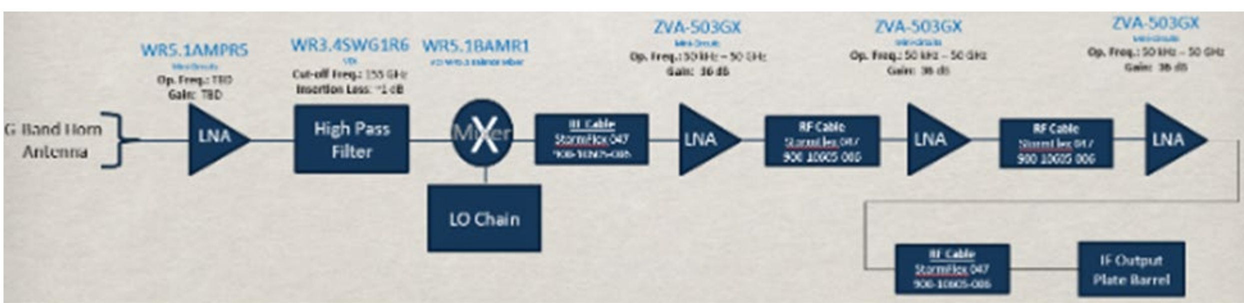

The simulation uses the amplitude and phase of passive component S-parameters as inputs to the noise-wave model, as well as certain noise parameters for active components. For the LNA and high-pass filter, only S-parameter amplitude information was available, so artificially generated phase information was used for the noise-wave model. Estimates of the amplifier noise characteristics also had to be generated, as the information needed for the model is not typically provided through manufacturer datasheets or test data. A measurement of the antenna’s input impedance (S11) was made; the antenna was further modeled as a two-port device to include potential reflections from the external calibration targets. The values used for the antenna’s S12, S21, and S22 were also artificially generated to enable this. Finally, the calibration targets and analog-to-digital conversion (ADC) of data were modeled as terminations, with the ADC assumed to be a perfect 50-ohm termination. The calibration target reflection coefficients were estimated and converted to an input impedance that connects to the two-port antenna component in the model. Due to the number of estimated/generated inputs to the model, the model is not expected to precisely reproduce the recorded data from the instrument, but rather serve as a radiometer analogue to explore potential wideband/standing-wave effects that could arise in the HyMPI instrument.

Measured versus simulated data: A lab test (Figure 23) of the HyMPI radiometer measured a fixed cold target (open dewar of liquid nitrogen) and a hot target at 4 different distances from the antenna: 12.65, 22.65. 42.65, and 44.65 mm. In a traditional radiometer model, the distance of the target from the antenna should have minimal impact on the measured results, only having an impact based on the antenna pattern and the proportion of the pattern that the target occupies. In the noise-wave model, the apparent impedance of the calibration target based on its reflection coefficient will impact the standing-wave effects seen by the radiometer, changing the apparent brightness temperature observed as a function of frequency.

Figure 23: Calibrated hot load brightness temperatures with the hot load at four different distances from the antenna

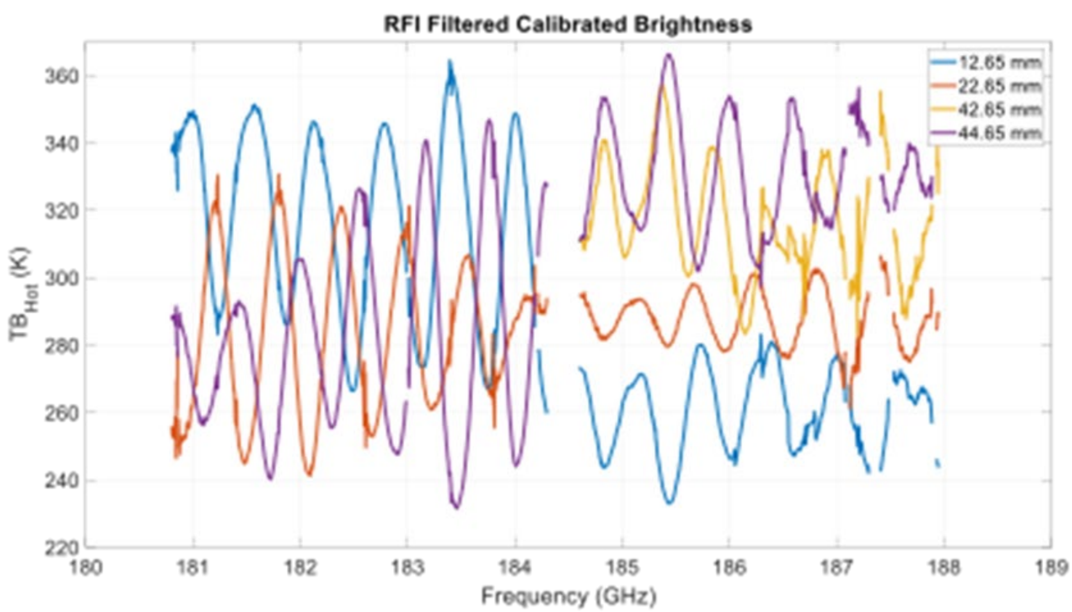

The average power received from the hot target at the four different distances was averaged together to make one composite hot measurement. A calibration curve using this composite hot measurement and the measurement of the cold target was generated, and then the temperature of the hot target at each distance was recalculated using this composite calibration curve. The results show a significant standing wave effect in the retrieved temperature data, indicating that the distance of the hot target changed the received power of the radiometer and that standing waves occur due to reflections from the target.

The data was recorded by two distinct ASICs (half of the bandwidth recorded per ASIC), each of which showed a slightly different effect. Observing the standing wave pattern in the measured data, the frequency of the standing wave for each ASIC was calculated and converted to an apparent electrical length based on a reflecting target. Figure 24 plots this apparent distance versus the hot target distances and shows an average "offset" distance of the instrument of approximately 200 mm. This offset distance accounts for the physical length of the instrument as well as any electrical delays introduced.

Figure 24: Apparent distance to reflection from calibrated data (symbols) plotted versus actual distance to target

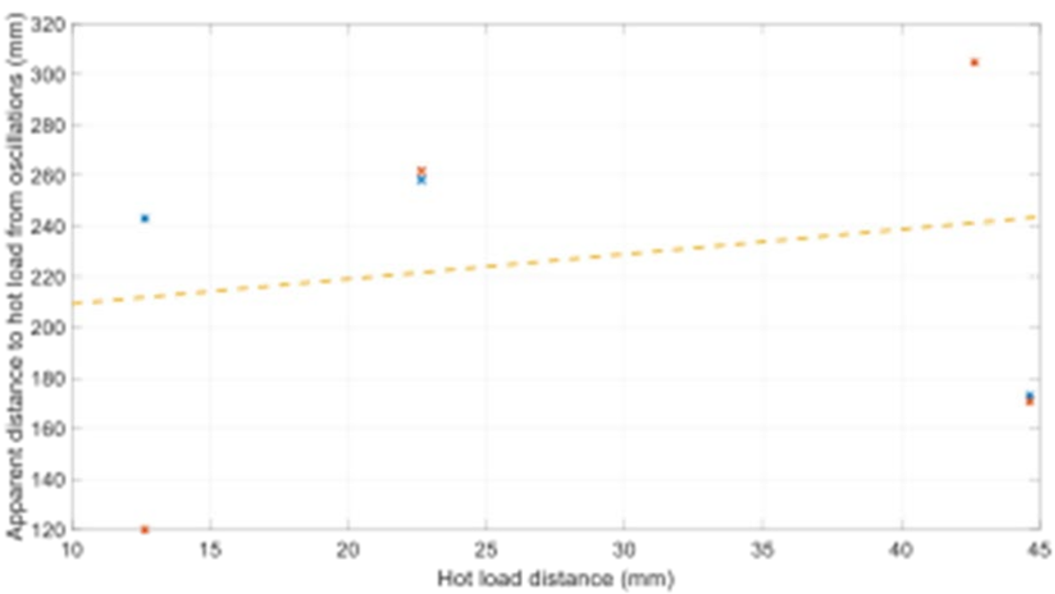

A noise-wave simulation of the system was conducted using the offset distance (200 mm) as the physical length of the two-port model of the antenna. Setting the cal target reflection coefficient to 10 dB results in a similar impact on receiver temperatures as was seen in the recorded data (Figure 25). One ASIC shows a significantly higher oscillation magnitude than the other, indicating that the termination of the model likely needs further refinement. In the future, detailed measurements of every component can help to improve the accuracy and fidelity of the noise-wave model

Figure 25: Noise wave model outputs for four calibration target distances (red) compared with measurements (blue)

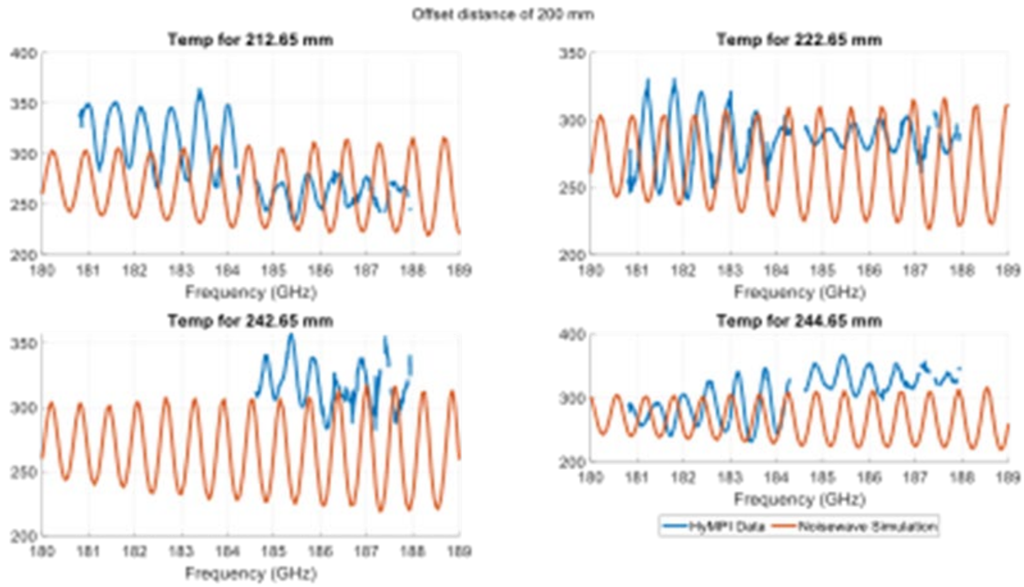

In a real system, there is likely to be a single hot and cold target at fixed positions, but the observed target may be at a different distance (e.g., observing the Earth compared to two on-board calibration targets as with COSMIR-H). A noise-wave simulation of this scenario was also conducted (Figure 26) to show the observed brightness for a 290 K target observed at different distances and different calibration target reflection coefficients/distances. The results for identical cal targets at identical distances are pictured below and show that the observed brightness of the moving target can have significant variation around the average brightness, varying with frequency. These standing-wave effects will average out when integrating over bandwidth, but hyperspectral observations would need to account for such effects through the use of higher fidelity models that include phase information in the calculated brightness temperature.

Figure 26: Noise wave simulations of received powers and associated brightness for objects at differing distances from the antenna

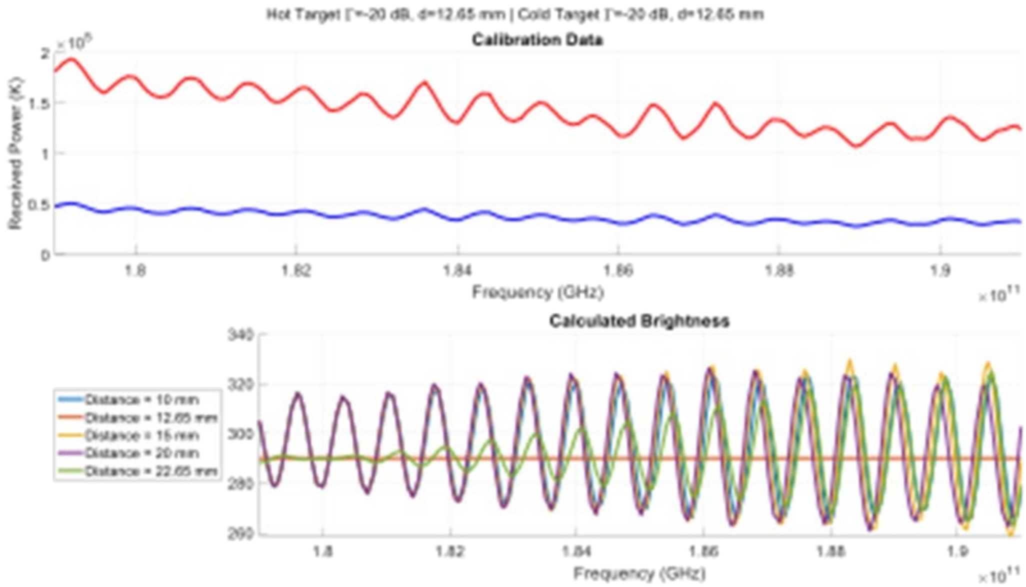

4. Community Radiative Transfer Model

4.1. Model Description

The Community Radiative Transfer Model (CRTM) is a fast and accurate all-sky radiative transfer model for the computation of passive satellite radiometer radiances and their corresponding K-Matrix Jacobians ([6, 8]). The CRTM is widely used for remote sensing and satellite data assimilation tasks in research and operations.

4.2. CoSMIR-H CRTM Coefficients

The development of the CoSMIR-H instrument coefficients for the CRTM is detailed in the corresponding project report ([7]) and summarized in the following. The full resolution instrument configuration with over 6000 channels was split up into 6 coefficient sets for the coefficient generation process. These binary coefficients are used as input to the radiative transfer model to generate the observations required by other members of the instrument team. The coefficients were generated based on the spectral information, including the channel center frequency, bandwidth, and polarization provided by the instrument team. The spectral response function (SRF) of each individual channel was assumed to have a generic boxcar shape, as we do not have detailed measurements of the SRF. It should be noted that wider band channels sometimes show significant variation across the channel passband, however. The spectral range of the individual instrument coefficient sets is given in Table 4. The first two coefficients (COSMIR-H1and COSMIR-H2) cover the temperature sounding channels near 60 GHz, the third co-efficient set (COSMIR-H3) covers the window channels near 90 GHz, and the last three sets (COSMIR-H4, COSMIR-H5, and COSMIR-H6) cover the water vapor channels near 183 GHz.

Table 4: Frequency range for different sets of CRTM specific spectral and transmittance coefficients.

Coefficient	cosmir-h1	cosmir-h2	cosmir-h3	cosmir-h4	cosmir-h5	cosmir-h6
Minimum Frequency [GHz]	50.0	53.92	89.00	175.31	180.77	186.24
Maximum Frequency [GHz]	53.91	57.99	165.30	180.77	186.77	191.30

5. OBS – CALC Demonstrations

CoSMIR-H instrument performance during WH^{2}yMSIE was evaluated by differencing observed (CoSMIR-H) Tbs and calculated TBs derived from CRTM simulations that used weather and reanalysis model data as input (hereafter, referred to as "obs-calc"). As part of this effort, CRTM generated three sets of calculated TBs using meteorological data (e.g., air temperature, specific humidity, geopotential height, wind, air pressure, among other key variables) from three different models, which includes NOAA's High Resolution Rapid Refresh model (HRRR), Goddard Earth Observing System - Forward Processing model (GEOS-FP), and Modern-Era Retrospective Analysis for Research and Applications, Version 2 model (MERRA-2). To permit direct comparison among these models, improve data read times, and simplify ingesting each into CRTM, all three models were co-registered into a common 3-km horizontal latitude-longitude grid covering the entire region sampled by the WH^{2}yMSIE campaign (See Figure 9). For the sake of brevity, the obs-calc results shown section below are solely on HRRR, given its higher native spatiotemporal resolution (3-km grid spacing, 1-hour output) relative to GEOS-FP and MERRA-2 (27-km grid spacing, 3-hourly output). For simplicity and consistency with the figures presented in this section, we will re-fer to CRTM-simulated HRRR data as "CRTM_HRRR". This section will describe our data filtering methodology, our approach to deriving our cloud masks, show composite probability density functions (PDFs), and finally show spectral analysis plots that show CoSMIR-H to model TB bias, their associated standard deviation, and how they compare to nominal instrument noise (i.e., noise equivalent delta temperature (NEDT)).

Airborne microwave TB retrievals can face numerous challenges, especially those associated with clouds and land surface emissivity, in addition to instances of bad data (i.e., missing values) and times when the aircraft was not level. To address these challenges and mitigate their impact on our obs-calc bias estimates, all CoSMIR-H and CRTM_HRRR TB data are filtered using the five different filters described in Table 5; additionally, CRTM was run in "clear sky" mode to simulate TBs without clouds present. To filter out lower quality CoSMIR-H data, over land data flight segments, and sections of the flight segment with excessive roll, only points where the CoSMIR-H quality flag had a value of 1, HRRR model land/ocean flag values had a value of 1,and where the ER-2 aircraft roll angle was ≤ 3º were kept. Cloud filtering was applied by filtering data using both HRRR-simulated cloud fraction and cloud coverage as derived from level 2 MASTER (MODIS/ASTER Airborne Simulator) data, which is a 50 spectral band imager covering the visible, near-infrared, shortwave infrared, and thermal infrared with an average pixel resolution of 15 meters and has a roughly 115-km wide scan width and flew with CoSMIR-H on-board the NASA ER-2 aircraft. To help illustrate these various cloud data, Figure 27 depicts raw MASTER level 2 cloud mask, HRRR cloud fraction, CoSMIR-H 89 GHz horizontally polarized (H) TB,s and MASTER-based cloud fraction co-registered to the nominal 2.4-km footprint of CoSMIR-H. MASTER-based cloud fraction was retrieved by summing the cloudy MASTER pixels within each CoSMIR-H footprint and dividing it by the total number of MASTER pixels with each CoSMIR-H footprint. As can be seen in Figure 27 panel 3, CoSMIR-H 89-GHz H TBs correspond well to the MASTER-based cloud fraction, which motivate the use of 89-GHz H, 89-GHz vertically polarized (V), and 191-GHz V TB data to help further mitigate cloud contamination risks given the sensitivity of each of these frequencies to ice-phase clouds via sigma filtering.

Unlike the other four filtering methods, the sigma filter applied in this obs-calc demonstration is derived from a composite of all flight segments after all the preceding filters in Table 5 were applied. The sigma filtering method further mitigates ice-cloud contamination and large-scale outliers by filtering all 6,148 CoSMIR-H channels using obs-calc data (CoSMIR-H - CRTM_HRRR) TB data at 89-GHz H, 89-GHz V, and 191-GHz V only. For this method, obtained obs-calc data at these three frequencies, identified the local peak in the obs-calc data, and then derived a at each frequency

where $$\sigma = \frac{0.5 * \text{fwhm}}{\sqrt{\ln 2}},$$

and fwhm is the full-width half peak height. Once σ is calculated, we save this value along with the corresponding obs-calc value matched to the composite PDF peak. In our initial work, we found needed to be derived from a composite of multiple flight segments due to the high degree of variability among the individual flight segments, due to changes in the atmospheric state and, in particular, atmospheric water vapor. A composite creates a more averaged and representative value by which to filter the TB data by effectively dampening data noise. In practice, the filter is applied to the TB data by removing all data points where obs-calc TBs for each flight segment exceed +/- from the composite peak at 89-GHz H, or 89-GHz V, or 191-GHz V.

Figure 27: Cloud and brightness temperature analysis depicting the raw MASTER level 2 cloud mask, MASTER cloud fraction scaled to CoSMIR-H footprints, HRRR total cloud fraction, and CoSMIR-H 89-GHz TB from an over ocean flight segment around 22:41 UTC on 07 Nov. 2024 WH^{2}yMSIE flight

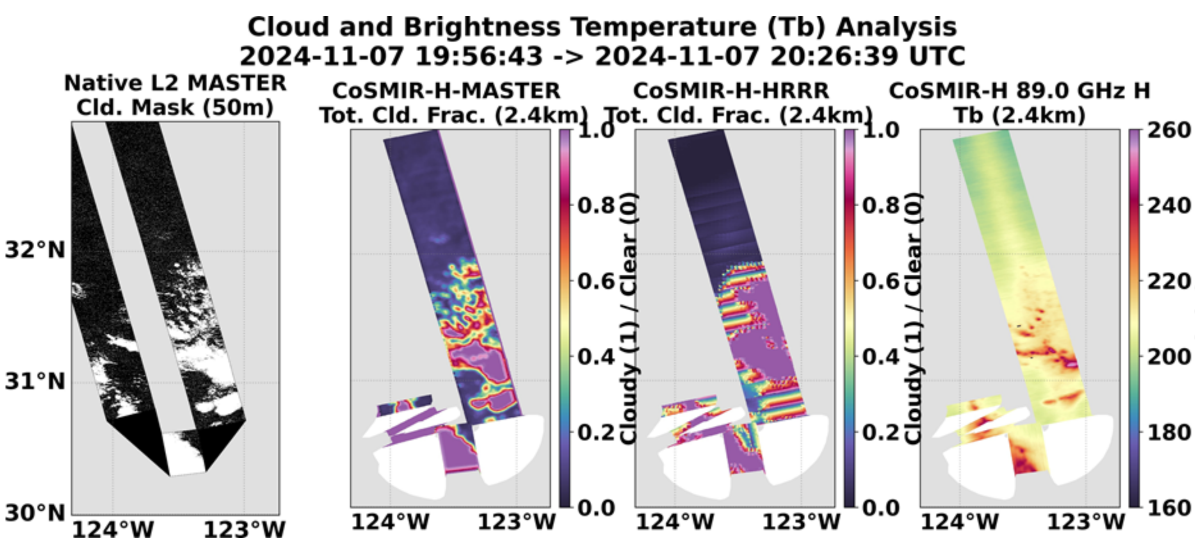

Airborne microwave TB retrievals can face numerous challenges, especially those associated with clouds and land surface emissivity, in addition to instances of bad data

Table 5: Filtering criteria for CoSMIR-H and CRTM model TB obs-calc analysis

Filter	Criteria	Rationale
QC	QC Flag = 0	Remove low-quality data (flag =1)
Surface	Ocean Flag = 1	Remove land (emissivity errors)
Clouds	≤ 3º	Remove excessive roll data
Sigma	Remove > 1σ from 89 GHz (H/V), 191 GHz (V) $\sigma = \frac{0.5 * \mathrm{fwhm}}{\sqrt{\ln 2}}$	89/191 GHz ice-sensitive; 1σ removes outliers. Ensures clear-sky scenes. Fwhm= full-width half max

To illustrate the filter method and the effectiveness of our cloud filtering approach, Figures 28 - 33 show composite PDFs at 89-GHz H, 89-GHz V, and 191-GHz V in sets both without and with cloud filtering applied. Each of these figures depicts the composite obs-calc PDFs at the specified frequency, both before (black line) and after (red line) the composite filter is applied, and the corresponding dataset mean is shown as a solid line.

Without cloud filtering applied, Figure 28 shows the sensitivity of the 89-GHz H channel to ice clouds given the long and extended tails in the raw obs-calc data (black line). Once the filter is applied, these extended cold and warm tails are cut off abruptly at -7.5 and 2.5K, respectively. While applying a did help to curtail the obs-calc data tails, it became clear that when it is compared to Figure 29, where the obs-calc Tbs apply MASTER- and HRRR-based cloud filtering, that in Figure 28 still has a significant degree of cloud contamination in the PDF. In contrast, Figure 29 presents a composite 89-GHz H composite PDF that is much sharper and narrower even before the , with a range of obs-calc Tbs from -5.0 K to 0.1 K, and cuts the value from 5.06 K to 2.6 K after the filter is applied. The narrowing of the data distribution and notably smaller values demonstrate the effectiveness and importance of cloud filtering to obtain the clear-sky scenes to mitigate cloud-related errors and extract more accurate estimates of potential bias in CoSMIR-H TBs.

Figure 28: Composite probability density functions (PDFs) of 89-GHz horizontally (H) Obs-Calc using all over-ocean WH^{2}yMSIE flight segments. The thick black and red lines show the composite PDFs before and after the sigma filter is applied, respectively, and the solid vertical lines depict mean values, and the dashed lines show the half peak heights for these data.

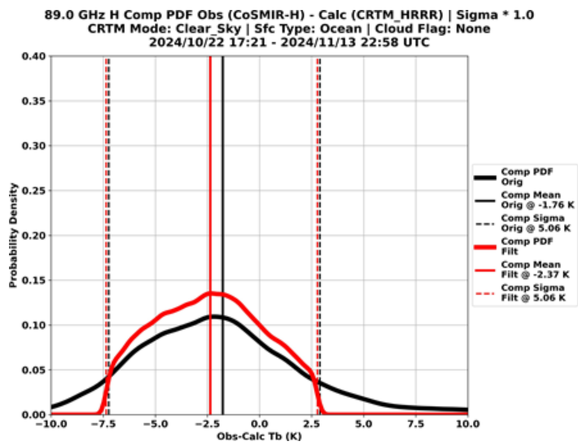

Figure 29:Same as Figure 28, but with MASTER and HRRR cloud filtering applied.

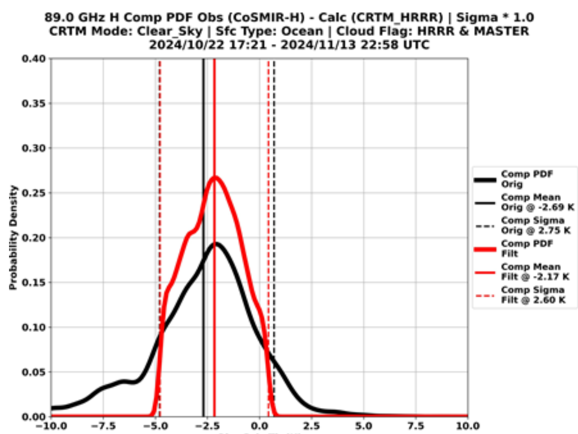

Figures 30 and Figure 31 show the same application of the filter both without and with cloud filtering, but for 89-GHz V. Because both 89-GHz H and V are at the same frequencies, but differ in their polarization only, the 89-GHz V composite TB PDFs look remarkably similar to their 89-GHz H counterpart aside from a slightly narrower PDF distribution and once again demonstrate the notable impact of cloud filtering to the resulting value (3.55 K reduced to 1.81 K).

Figure 30: Same as Figure 28, but for 89-GHz vertically (V) polarized Obs-Calc (CoSMIR-H - CRTM-simulated HRRR) TBs.

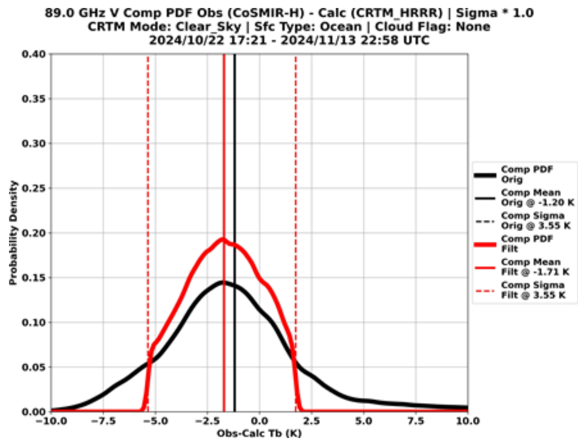

Figure 31: Same as Figure 30, but with MASTER and HRRR cloud filtering applied.

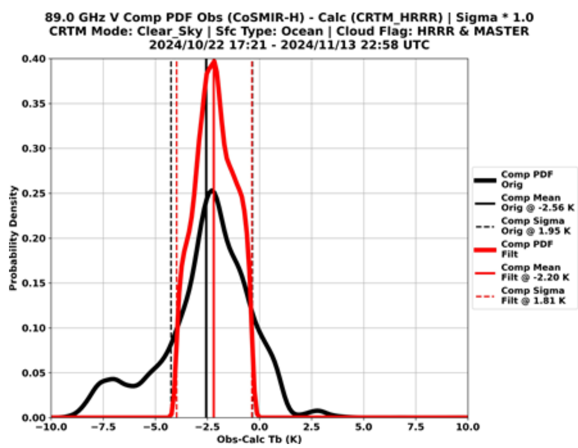

Finally, 191-GHz V was selected for filtering due to its position as a shoulder frequency that is both near the surface and quite sensitive to ice clouds and is presented both without (Figure 32) and with (Figure 33) cloud filtering applied. As compared to 89-GHz, the 191-GHz channel presents symmetric composite TB PDFs that are centered much closer to zero (0.73 K vs 02.17 K). Applying a Figure 39 to both composite PDFs mitigates the cold and warm tails, but the impact of cloud filtering is not a profound as at 89 GHz, but it still has a notable impact on the cold tail.

Figure 32: Same as Figure 28, but for 191-GHz vertically (V) polarized Obs-Calc (CoSMIR-H - CRTM-simulated HRRR) TBs.

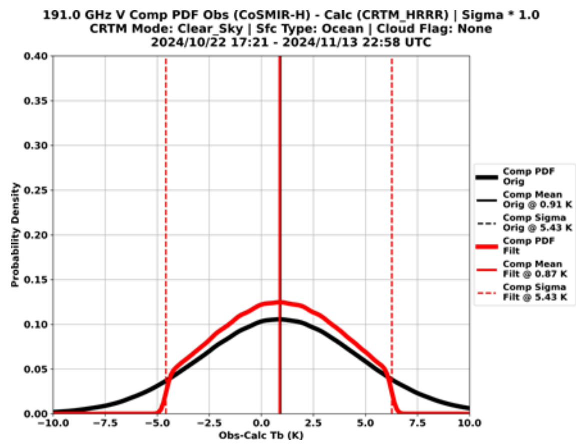

Figure 33: Same as Figure 32, but with MASTER and HRRR cloud filtering applied.

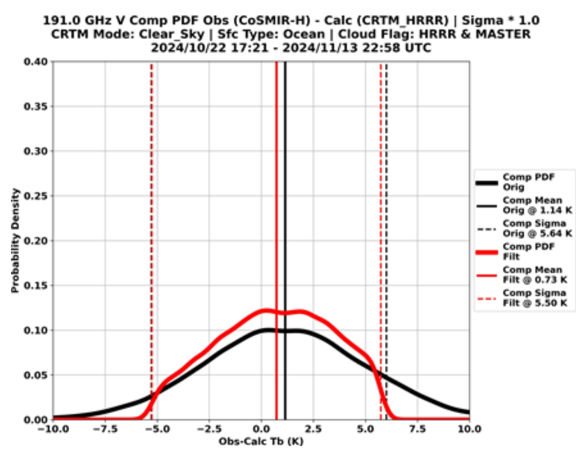

Figures 34 - Figure 39 showcase how both cloud filtering and the filter impact the composite PDFs of CoSMIR-H and CRTM_HRRR TBs, and each PDF compares to the other. Starting at 89-GHz H, Figure 34 shows both sets of composite TB PDFs present PDF distributions of similar magnitude and range of TBs. Once HRRR- and MASTER-based clouds are removed, both sets of TBs still show similar PDFs to each other, but when comparing the corresponding PDFs without cloud filtering, a clear reduction TBs above 200 K is observed, which clearly demonstrates the removal of clouds from the dataset (TBs for ice clouds at 89-GHz present warmer TB values). However, both the cloud and no cloud PDFs show the calculated (i.e., CRTM_HRRR) TBs to be offset toward slightly higher TBs relative to those from CoSMIR-H, which suggests a potential bias. Unlike the obs-calc composite PDFs at 89-GHz V (i.e., Figures 30 and Figure 31), the appearance and distribution of composite TB PDFs for CoSMIR-H and CRTM_HRRR TBs at 89-GHz V vary considerably from 89-GHz H, which, given that both 89-GHz H and V are filtered identically, is solely a result of their respective polarizations. Despite the difference in the appearance of their composite PDF distributions, it can be seen that cloud filtering similarly reduces warm TB values from CoSMIR-H and CRTM_HRRR and that CRTM_HRRR TBs tend to be offset toward slightly warmer TBs relative to CoSMIR-H. Finally, at 191-GHz V, both the CoSMIR-H and CRTM_HRRR TBs composite TBs are seen to be relatively comparable in width to 89-GHz H, but with a much higher PDF peak. Similar to the 191-GHz obs-calc composite PDFs, HRRR- and MASTER-based cloud filtering show a reduction in TBs above 282K, which shows the removal of ice-phase clouds, but unlike for 89-GHz, CRTM_HRRR TBs composite PDF tends toward slightly lower TB values.

Figure 34: Composite PDFs of 89-GHz horizontally (H) polarized TBs from CoSMIR-H (black line) and CRTM_HRRR (1-sigma filter, red line) with no cloud filtering applied from all over-ocean WH^{2}yMSIE flight segments.

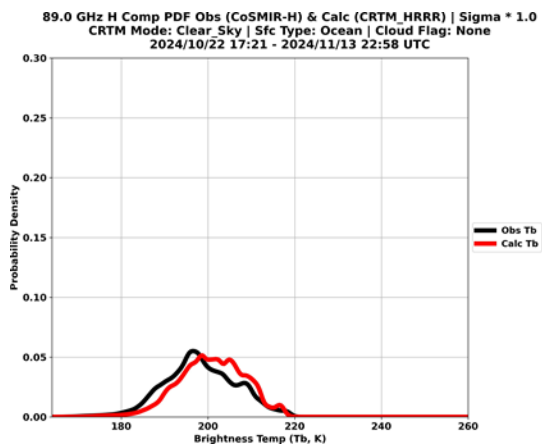

Figure 35: Same as Figure 34, but with MASTER and HRRR cloud filtering applied.

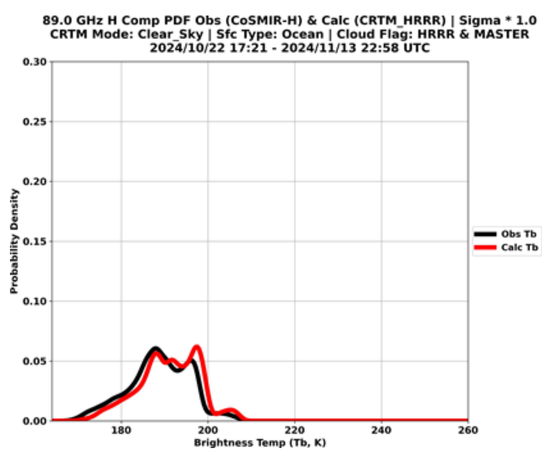

Figure 36: Same as Figure 34, but for 89-GHz vertically (V) polarized TBs.

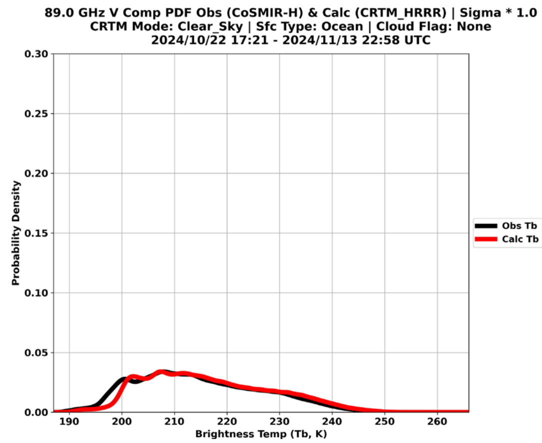

Figure 37: Same as Figure 36, but with MASTER and HRRR cloud filtering applied.

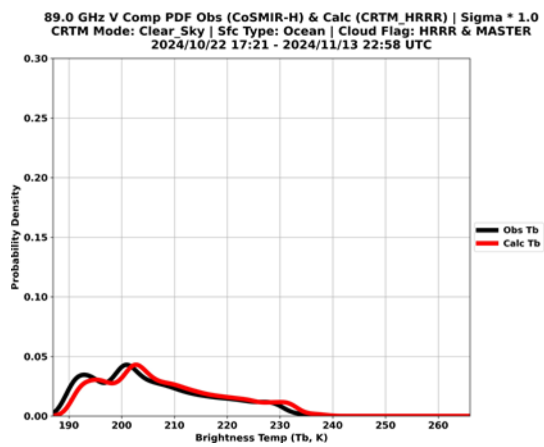

Figure 38: Same as Figure 34, but for 191-GHz vertically (V) polarized TBs.

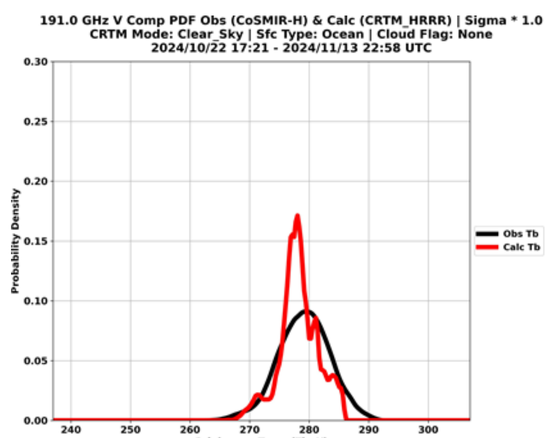

Figure 39: Same as Figure 38, but with MASTER and HRRR cloud filtering applied.

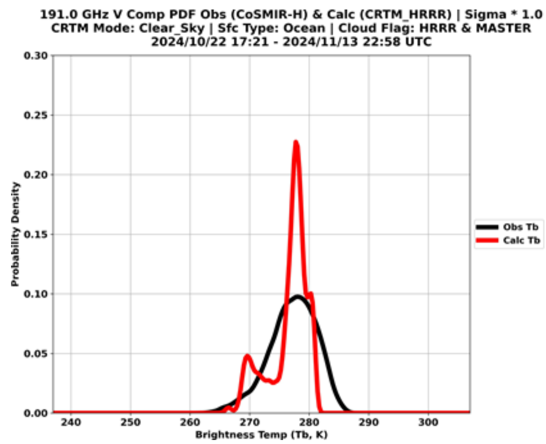

After applying the five filters to the obs-calc, CoSMIR-H and CRTM_HRRR TBs as described in Table 5 and as detailed above, Figures 40 - 43 show the resulting composite bias and standard deviation analysis when applied across the hyperspectral oxygen (50-58 GHz) and water vapor (175-191 GHz) channels. Given that TB dataset has three dimensions (frequency, incidence angle, and time), we carried out a dimension reduction by time averaging or via standard deviation, which allows the generation of figures highlighting potential biases and to compare instrument bias to instrument noise (i.e., NEDT). Figure 40 shows the composite mean spectral analysis for 50-58 GHz, which shows time-averaged CoSMIR-H Tbs and obs-calc TBs as a function of incidence angle. As seen in the CoSMIR-H TBs (top panel), CoSMIR-H TBs are highest around 53 GHz and coolest above 55 GHz, and show some contamination from the hot and cold targets towards the edge of the scan. When compared to CRTM_HRRR TBs across the entire scan (middle panel) and at nadir (red line, bottom panel), it is seen that CoSMIR-H TBs exhibit up to a 6K (50.8 GHz) warm bias at surface-seeing channels below 52.8 GHz. This warm bias is likely associated with a combination of factors, including surface emissivity applied in CRTM, HRRR wind errors, and potential bias in the CoSMIR-H TBs. At frequencies above 52.8 GHz, the obs-calc TBs differences tend to be considerably smaller and closer to zero. Errors in the handoff regions between the two application-specific integrated circuits (ASICs) lead to missing data around 54 GHz, which are filtered out by the COSMIR-H QC flag. Figure 41 presents the same CoSMIR-H TB data as Figure 40, but replaces the mean obs-calc TBs with their standard deviation (middle panel), which permits comparison of the variance in obs-calc Tbs to COSMIR-H's nominal NEDT (1.2K between 50-58 GHz). As compared to the mean obs-calc TBs, the obs-calc standard deviation plot is considerably nosier and also shows evidence of CoSMIR-H cold and hot target contamination near the scan edges (especially around -46.0).Additionally, cross scan variability shows evidence of data striping at particular incidence angles (i.e., -30 , 15 , 40). However, despite the obs-calc TB warm bias from CoSMIR-H, the standard deviation of obs-calc TBs is of similar magnitude or even smaller than NEDT. Therefore, even with the potential high TB bias in CoSMIR-H below 52.8 GHz, the variance in the obs-calc TBs is relatively consistent across the entire oxygen band suggesting that the potential bias in CoSMIR-H is likely more systematic in nature.

Figure 40: Composite mean spectral analysis of CoSMIR-H hyperspectral oxygen band (50-58 GHz) from all over-ocean WH²yMSIE flight segments. Panels show (top) mean CoSMIR-H TB and (middle) Obs-Calc TB differences (CoSMIR-H - CRTM_HRRR) as a function of instrument incidence angle, and these same two quantities at nadir (CoSMIR-H TB, blue line; Obs-Calc, red line).

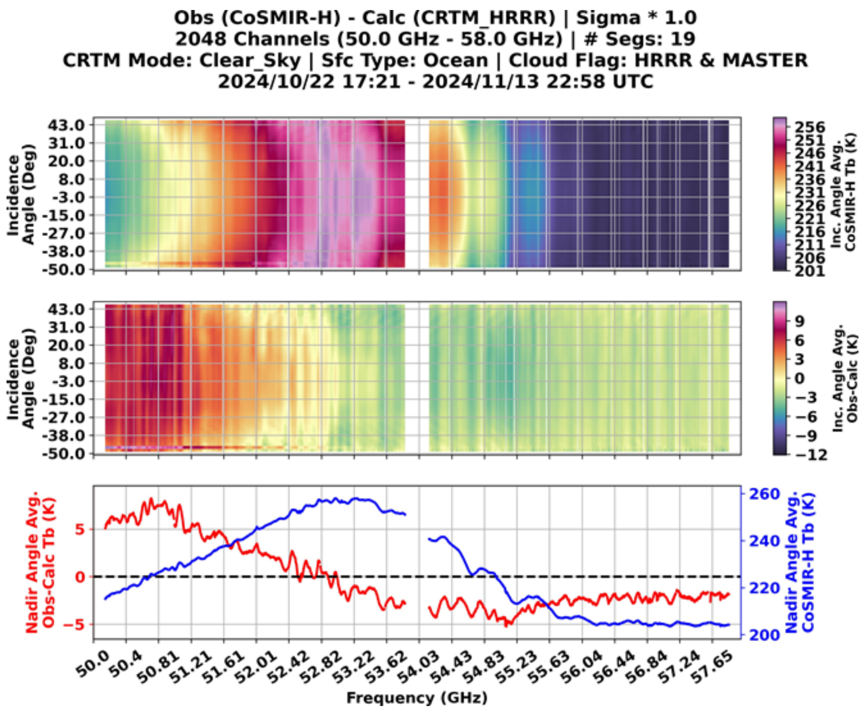

Figure 41: Composite spectral standard deviation analysis of CoSMIR-H hyperspectral oxy-gen band (50-58 GHz) from all over-ocean WH²yMSIE flight segments. Panels show (top) mean CoSMIR-H TB and (middle) standard deviation of obs-calc TB differences (CoSMIR-H - CRTM_HRRR) as a function of instrument incidence angle, and these same two quantities at nadir (CoSMIR-H TB, blue line;

standard deviation of Obs-Calc TBs, red line). Grey horizontal dashed line denotes CoSMIR-H nominal noise equivalent delta temperature (NEDT, K)

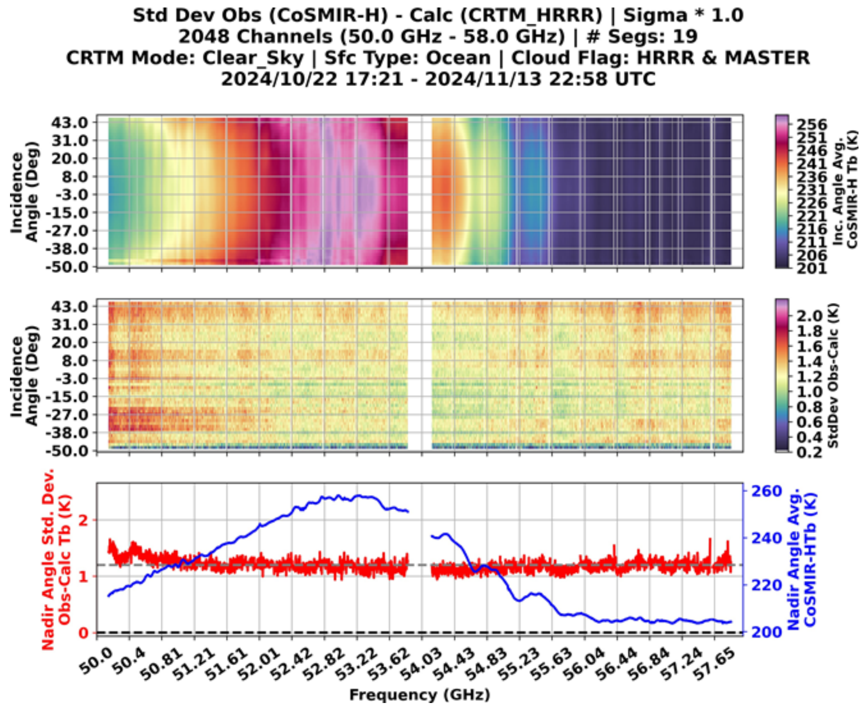

Figures 42 and 43 show the composite mean and standard deviation analysis for hyper-spectral water vapor channels (175-191 GHz). Figure 42 demonstrates that the water vapor band differs from the oxygen band by having a local TB minimum in the middle of the frequency spectra (~183 GHz) with the highest TBs occurring at the shoulder frequencies (≤ 179 GHz and ≥187 GHz). In contrast to the mean obs-calc TBs at 50-58 GHz, at 175-191 GHz, the mean obs-calc TBs tend to be comparatively smaller and lack a frequency dependence, yet the surface seeing, shoulder frequencies do show increased error towards the scan edges. More notably, and best illustrated with the nadir angle obs-calc Tbs (red line, bottom panel), the obs-calc Tbs tend to be much more flat (+/- 1K), yet there is a standing wave pattern that exists across the entire water vapor frequency spectra with around a 0.8 GHz periodicity and is particularly prevalent between 178 and 187 GHz. Because this standing wave pattern occurs at higher frequency bands this suggests this feature is likely attributable to 1/f noise and also other potential sources of error to include hot-cold load calibration of CoSMIR-H, or multi path interference, or perhaps errors with the CRTM-simulated TB data (such as those from wind) or a bias in CoSMIR-H TBs or any combination of the above. Due to having double the number of channels (4096 vs 2048), the water vapor spectra span 4 ASICs and similarly to the oxygen band the data quality in the handoff regions tended to be of poorer quality, resulting in 3 distinct zone of missing data near 179.3, 183.3, and 187.3 GHz. When replacing the middle and bottom panels of Figure 42 with the standard deviation (Figure 43) reveal that despite the presence of a standing wave pattern in the 175-191 GHz obs-calc Tbs, that the standard deviation of these same data does show these same pattern. Therefore, similar to the obs-calc TB biases at 50-58 GHz, the obs-calc TB differences in the water vapor band show consistent variance across the entire water vapor band and show no dependence upon frequency. Furthermore, the standard deviation of obs-calc Tbs at nadir are both relatively flat at or below the nominal CoSMIR-H NEDT (2.9 K) for almost the water vapor band. However, similar to the oxygen band results in Figure 41, the standard deviation obs-calc Tbs show evidence of hot and cold target contamination near the scan edges and data striping that varies as a function of incidence angle, which is likely associated with noise with the CoSMIR-H data.

Figure 42: Same as Figure 40, but for 175-191 GHz.

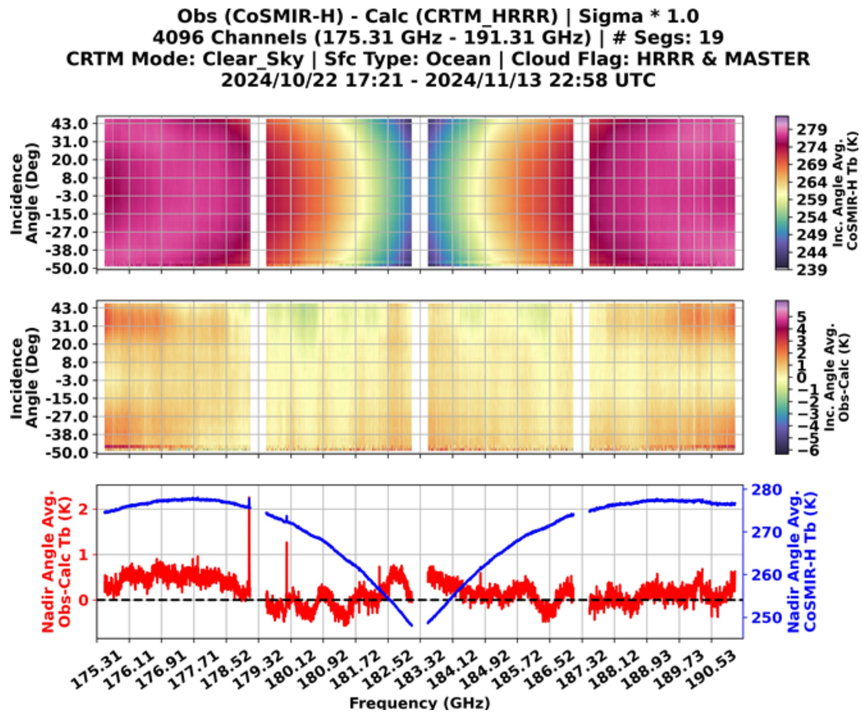

Figure 43: Figure 43: Same as Figure 41, but for 175-191 GHz.

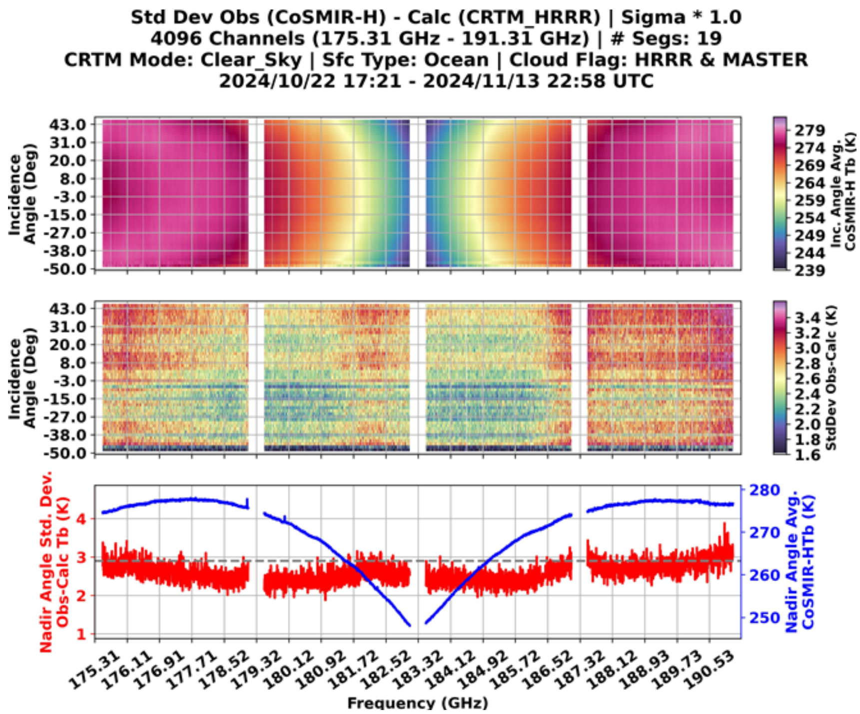

5.1. Apparent CRTM Oxygen Band Absorption Issues

The OBS-CALC validation between WH^{2}yMSIE observations and CRTM model out-put demonstrated apparent issues of the CRTM gas absorption model in the oxygen band between 50 and 60 GHz. An example of affected OBS-CALC results is given in Fig. 44. The Nadir angle-average OBS-CALC Tb results (red curve) show spikes around 56.84 and 57.65 GHz, initially indicating a problem in either observations or model. Further investigation identified the CRTM gas absorption model as the source of the problem. As shown in Fig. 45 for a hyperspectral MW test instrument, the CRTM optical depth output has a discontinuity in the vertical between roughly 55 and 115 GHz and around vertical atmospheric model layer 60. This discontinuity also affects other MW instruments, such as ATMS NPP, as shown in Fig. 46. The sharp vertical discontinuity in the CRTM optical depth of the affected channels is clearly visible.

Figure 44: Hovmöller-style plot of WH²yMSIE OBS-CALC results showing spikes in the nadir angle-average OBS-CALC T_b around 56.84 and 57.65 GHz (red curve).

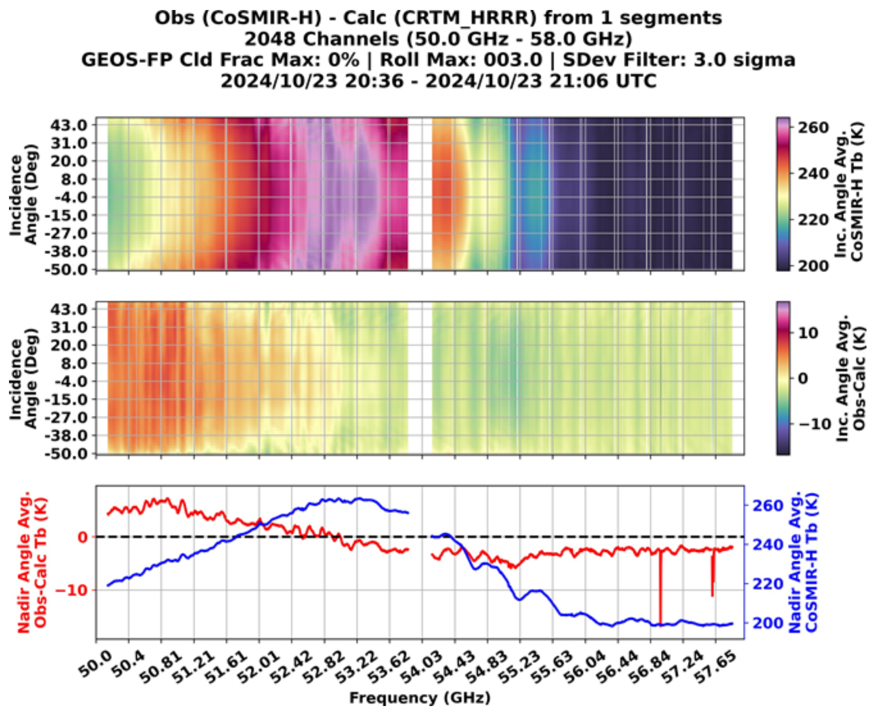

Figure 45: CRTM vertical optical depth profile spectrum in the 20 to 185 GHz MW region for a clear sky test profile.

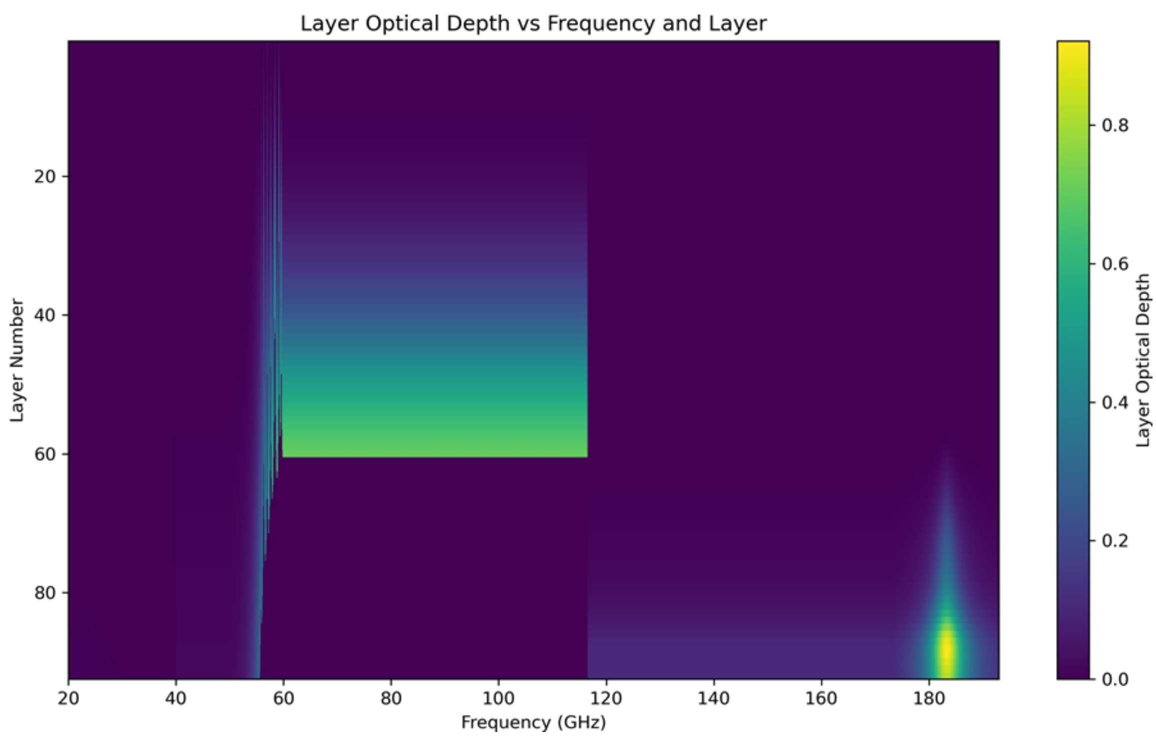

Figure 46: CRTM vertical optical depth profiles for ATMS NPP, channels 8-13. Vertical discontinuities are clearly visible. Aircraft level pressure is indicated as a dashed red line.

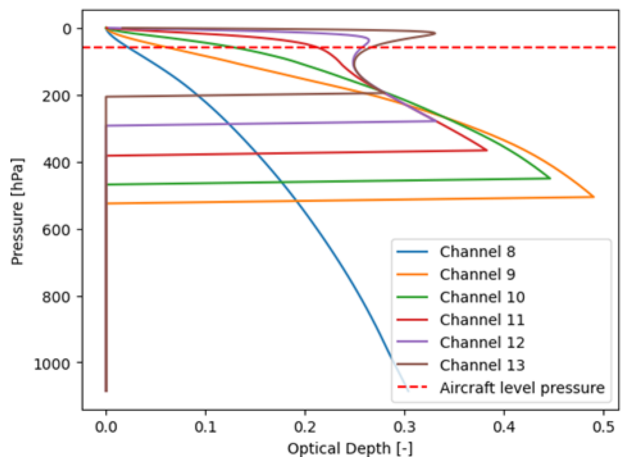

For comparison, the expected optical depth profile spectrum is shown in Fig. 47. This optical depth profile spectrum is computed using a rigorous MW line-by-line model, and does not show any discontinuities of the sort that are observed in Figs. 45 and 46.

Figure 47: Line-by-line radiative transfer model optical depth profile spectrum between 54 and 58 GHz.

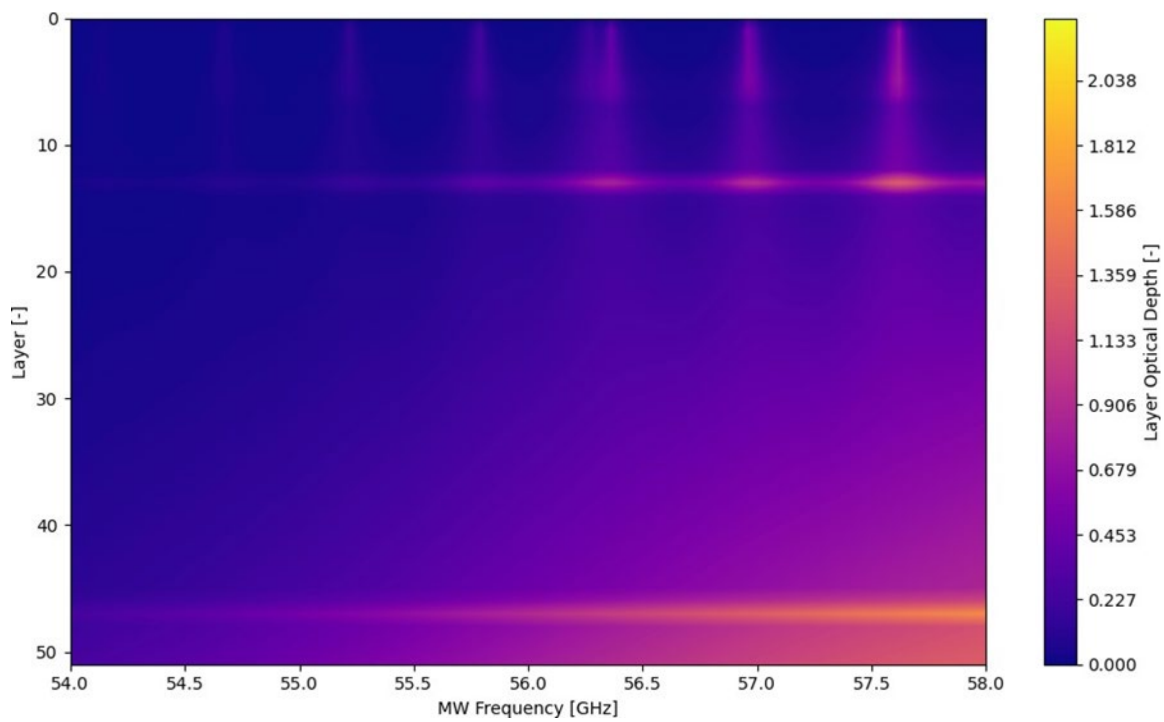

The affected CoSMIR-H WH^{2}yMSIE channels are:

– #1783 at 56.966797 GHz

– #1947 at 57.607422 GHz

– #1948 at 57.611328 GHz

– #1949 at 57.615234 GHz

This issue was reported to the CRTM core team at the Joint Center for Satellite Data Assimilation, and as of August 2025 is pending further investigation. The corresponding issue on the JCSDA/CRTMv3 repository ([5] [6]) is #224 with the title *apparent bug in oxygen-affected microwave bands*. As the problem does not exist in spectral regions dominated by water vapor absorption, it is likely related to the CRTM treatment of oxygen absorption in the MW region. The detection of this problem further demonstrates the value of WH^{2}yMSIE field campaign observations in assessing and validating model calculations.

6. Grouping Trade Studies

We conducted a trade study to perform channel grouping and evaluate its impact on maximizing the information content of hyperspectral microwave measurements. The goal of this analysis was to determine the optimal balance between spectral resolution and channel selection in order to reduce redundancy while still retaining the essential atmospheric signal. Brightness temperatures (TBs) were simulated from the Nature Run using MonoRTM at 3.9 MHz resolution, and correlation matrices were computed for the 50–58 GHz and 175–191 GHz bands. Figure 48 shows the correlation matrices for these two spectral regions of interest. A moving window with a high correlation threshold (0.9999) was applied to identify sets of highly correlated channels. Within each window, if multiple channels met the threshold, they were grouped into a single representative channel, with the center frequency chosen as the grouped channel and the bandwidth defined by the extent of the grouped set.

Figure 48: Correlation Matrix for the 50 GHZ band (left) and 183 GHZ band(right)

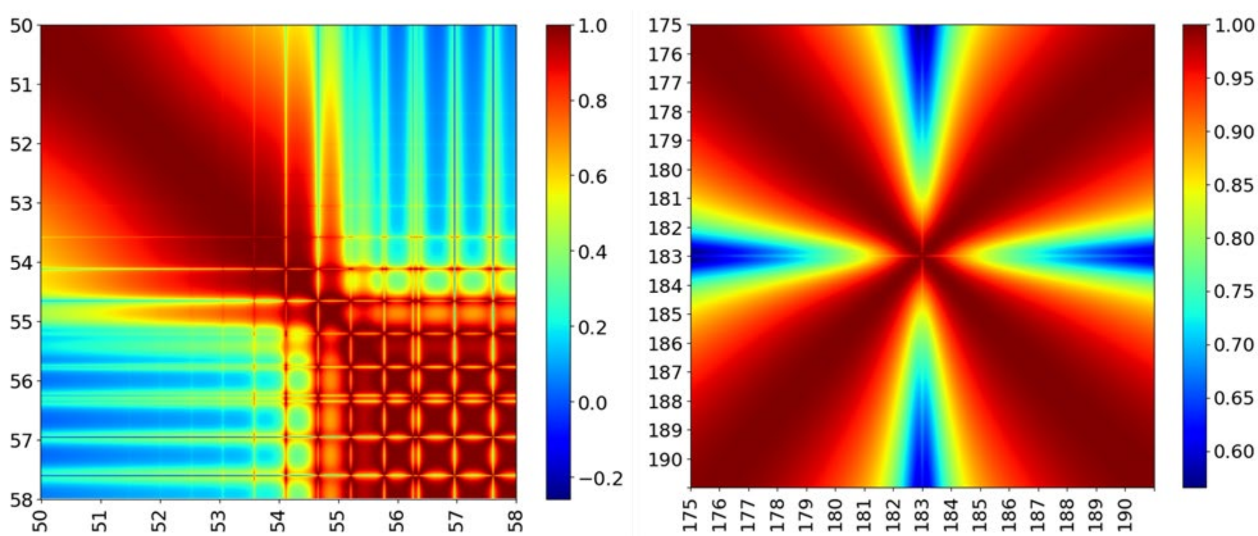

Applying this methodology, we assigned 466 grouped channels out of the original 2048 channels in the 50 GHz band and 614 grouped channels out of 4096 in the 183 GHz band. Figure 49 shows the resulting grouped channels, where each bar represents a grouped channel, with the width of the bar corresponding to its bandwidth and the y-axis indicating the number of native 3.9-MHz channels contained within each group.

Figure 49: Grouped channels for the 50 GHZ band (Top) and 183 GHZ band (Bottom), Each Bar represents a grouped channel and the width shows the bandwidth of each group

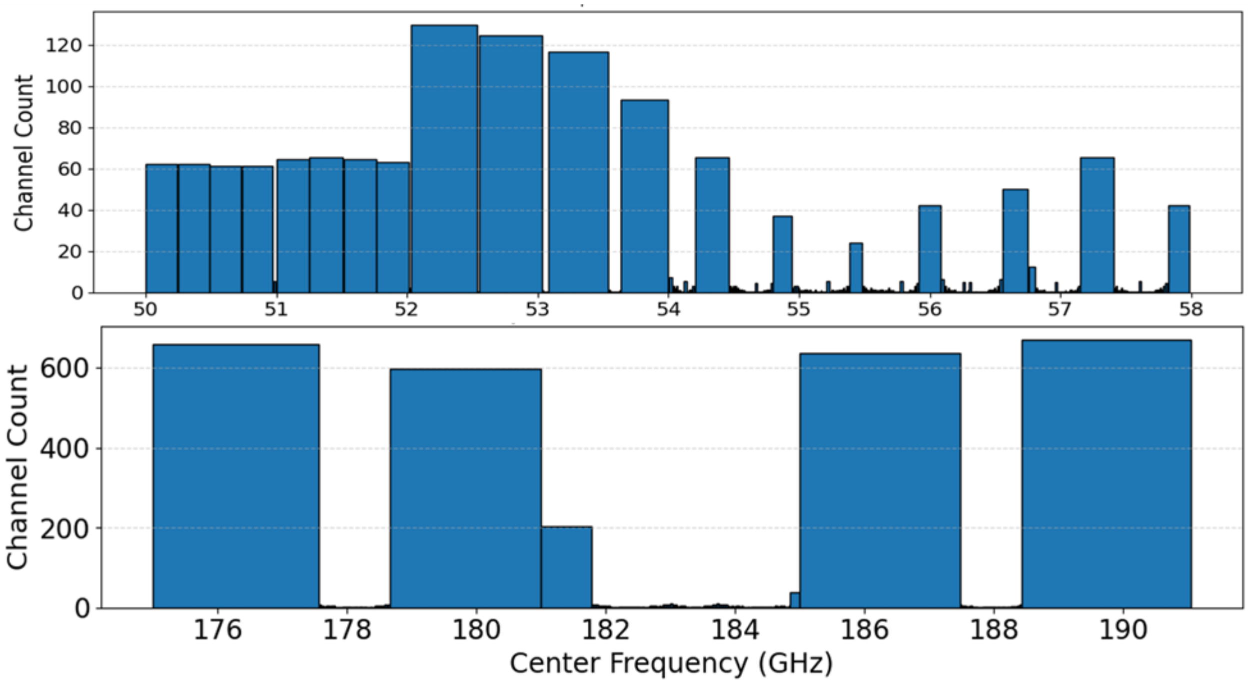

To validate the grouping, we reconstructed the full-resolution 3.9-MHz spectrum using a linear regression approach based on the grouped channels and compared it with the original spectrum. As shown in Figure 50, the reconstruction closely matches the original, with biases confined to ±0.2 K. The high fraction of variance explained demonstrates that the grouping effectively preserves spectral structure, while the standard deviation of differences remains below the recalculated Noise Equivalent Differential Temperature (NEDT) for the broader grouped channels. These results show that channel grouping effectively reduces redundancy while preserving measurement accuracy.

Figure 50: Error between the reconstructed and original (First row: Mean TBs, 2nd row: bias, 3rd row:variance Explained, 4th row: Stdv and NEDT, for 50 GHZ band (left) and 183 GHZ band(right))

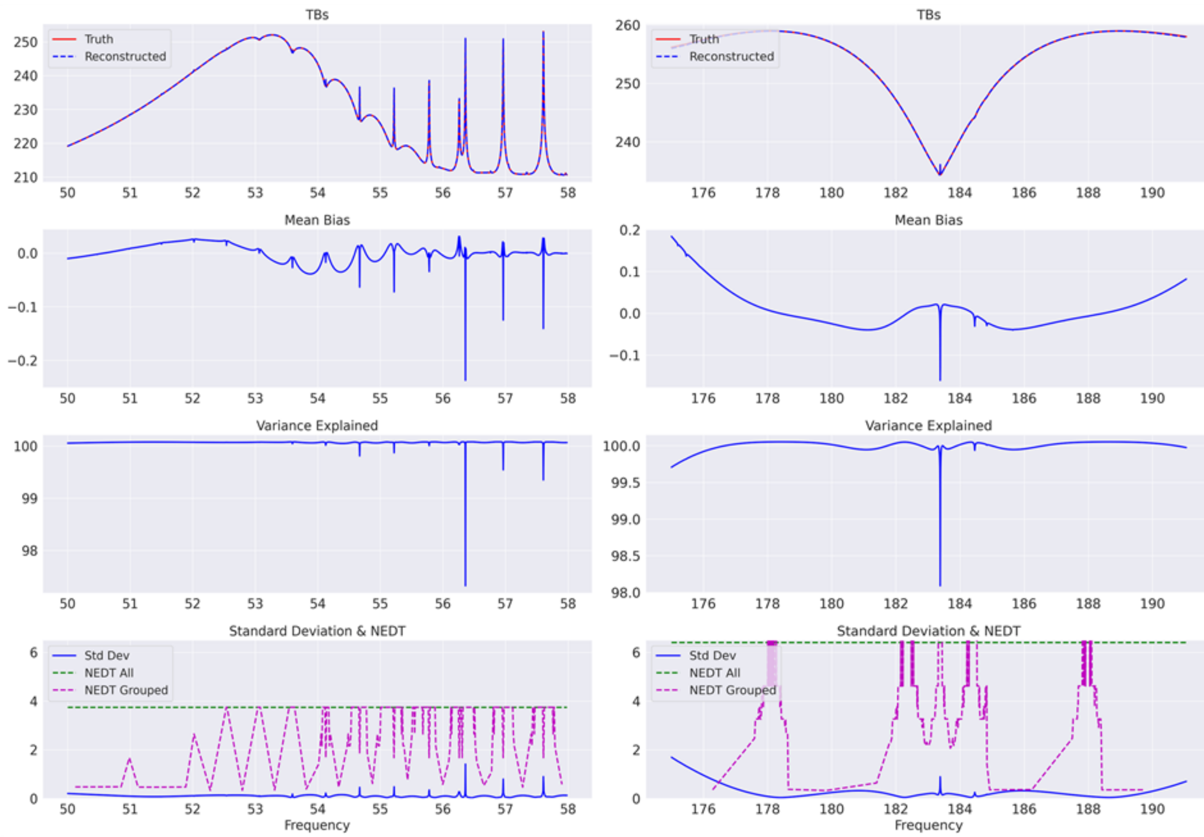

In addition, we applied a linear regression approach to predict temperature (T) and humidity (Q) profiles and compared retrievals obtained from the grouped channels with those using the original 3.9 MHz resolution (Figure 51). The top panels show the statistics for both T (left) and Q (right) before adding noise. For T, the RMSE indicates that grouped channels perform better below 950 hPa and above 850 hPa, whereas for Q, the full-resolution channels show slightly better performance than the grouped channels. After adding the corresponding noise (bottom panels), with noise levels recomputed for the grouped channels, both T and Q RMSE show improved performance when using grouped channels. These results demonstrate that, after accounting for the appropriate NEDT in the simulated observations, there is not only no loss of information content but also improved performance, since the grouped channels have lower NEDT, fewer channels with reduced noise, compared to the full-resolution case, which involves many more channels but higher noise levels. This provides confidence that the grouped channels effectively retain the essential atmospheric signal.

Figure 51: Regression Results predicting Temperature(left) and Humidity (right) using all channels vs grouped channels before (Top) and after (bottom) adding noise

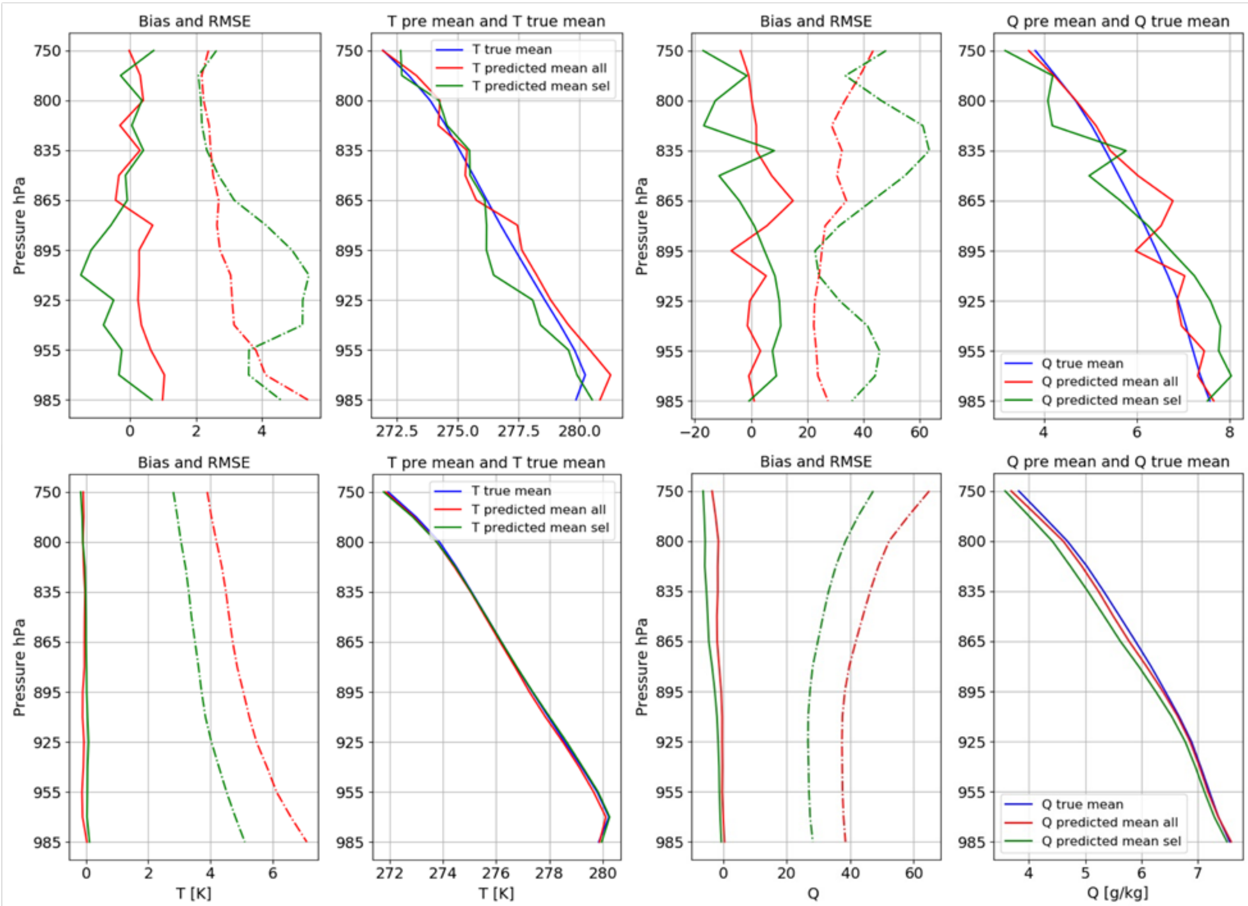

We plan to use these grouped channels in physical retrievals and data assimilation experiments, as most models cannot handle thousands of channels directly. Reducing the spectral dimension to roughly one thousand grouped channels will make the problem computationally feasible while still maintaining the information content for retrievals.

7 Recommendations for Space Concept

Hyperspectral Microwave (HMW) sensors have been strongly advocated by space and meteorological agencies to improve Numerical Weather Prediction (NWP) capabilities (Blackwell et al., 2011; Boukabara et al., 2011; Mahfouf et al., 2015; Aires et al., 2015, 2019) and enhance Earth’s Planetary Boundary Layer (PBL) observations (Teixeira et al., 2021; Gambacorta et al., 2023).

While conventional microwave (MW) sounders from the Program of Record (PoR) currently serve as the primary information source for NWP models — due to microwave radiation’s superior cloud penetration compared to infrared —their capabilities have been constrained by technological limitations. Traditional radiofrequency technology demands significant Size, Weight, and Power (SWAP) resources, which has restricted spaceborne MW sounding over the past five decades to only a few dozen sparse channels.

Photonic Integrated Circuits (PICs) and Application Specific Integrated Circuits (ASICs) are poised to revolutionize microwave sounding from space, enabling simultaneous, broadband, and hyperspectral measurements of Earth’s atmospheric microwave thermal radiation. The Hyperspectral Microwave Photonic Instrument (HyMPI) represents the first laboratory demonstration of PICs applied to hyperspectral microwave sensing and pioneers the development of the first space-based HMW sensor: the Advanced Ultra-high Resolution Optical and RAdiofrequency (AURORA) Pathfinder.

AURORA Pathfinder will measure the Earth’s thermal microwave spectrum in the 100-200 GHz range, which contains critical information in the Earth’s surface and atmospheric Planetary Boundary Layer, as well as atmospheric temperature, water vapor and hydrometeors. AURORA’s enhanced spectral coverage and resolution will significantly improve information retrieval regarding PBL thermodynamic structure and free tropospheric conditions. Furthermore, it will facilitate new scientific discoveries and validation opportunities in areas of high uncertainty that pose detrimental effects on PBL thermodynamic retrieval and numerical prediction capabilities, including water vapor continuum spectroscopy, surface emissivity, and hydrometeor properties (Figure 52). In this vein, AURORA Pathfinder will demonstrate mature technology readiness level (TRL) for a future NASA Planetary Boundary Layer mission. Findings from AURORA are also meant to inform NOAA and EUMETSAT next generation of microwave passive sounding programs.

Figure 52: This figure illustrates the brightness temperature (BT) spectrum across microwave frequencies (20-200 GHz) and contrasts three generations of microwave sounding technology: The Advanced Technology Microwave Sounder (ATMS), The Hyperspectral microwave Photonic Instrument (HyMPI) and the Advanced Ultra-High Resolution Optical and RAdiofrequency (AURORA) Pathfinder. This comparison describes the dramatic advancement from current sparse-channel microwave sounding to the comprehensive hyperspectral

capabilities of emerging photonic technologies, which will enable much more detailed atmospheric measurements and improved weather prediction capabilities.

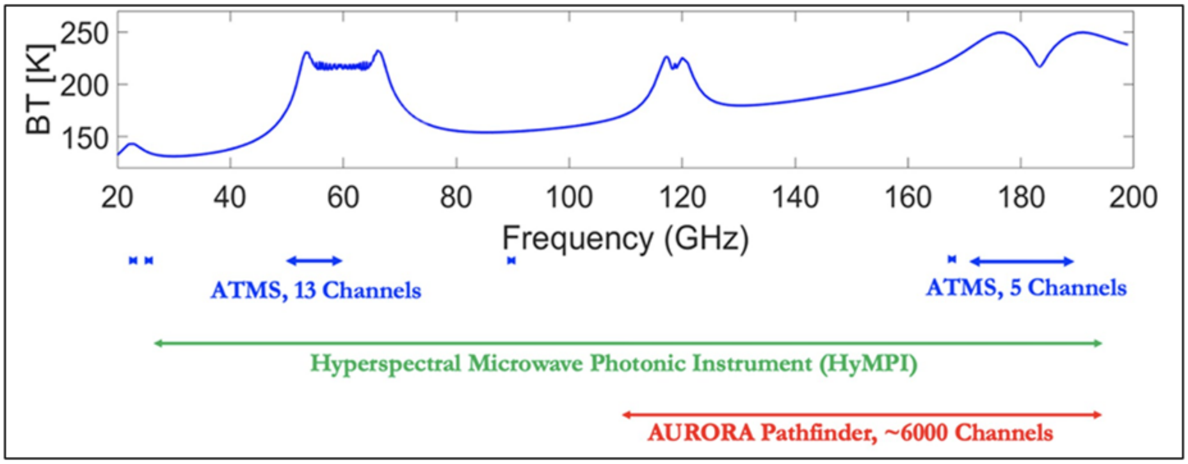

AURORA Pathfinder's mission is designed to demonstrate critical technologies in satellite operation, such as microwave PIC technology instruments in space, ASIC digital spectrometers in space, and on-board calibration of hyper and superspectral microwave payloads. It is scaled to the available funding resources, schedule, and the current technology status.

AURORA Pathfinder project objectives are:

1) Design and fabricate an end-to-end high-spectral resolution microwave sounder pathfinder instrument using photonic and digital spectrometer technologies;

2) Perform environmental testing and performance verification of the Pathfinder instrument demonstrating readiness for space flight;

3) Demonstrate calibration approaches for this advanced microwave sounder design;

4) Support spacecraft accommodation studies for a future flight demonstration;

5) Document lessons learned from the development/test phase for future digital and photonic spectrometer-based systems.

The AURORA Pathfinder project success criteria are:

1) End-to-end radiometric performance meets performance thresholds defined in the project requirements document;

2) The Pathfinder instrument successfully completes environmental testing and meets requirements as defined in the project environmental requirements document.

7.1. From HyMPI to AURORA Pathfinder and future Next Generation AURORA

AURORA Pathfinder builds on the technology readiness maturation of HYMPI (TRL= 4), which developed a modular instrument in the 160 – 200 GHz PBL spectral region. The overarching goal of the AURORA Pathfinder project is to advance HyMPI's TRL from 4 to 6, demonstrating its readiness for spaceflight and science demonstration.

HyMPI's photonic technology is agnostic to the spectral region. The use of multiple photonic modules like HyMPI will enable, in the future, full, contiguous coverage of the entire 200 GHz spectrum, leading to AURORA Next Generation for operational and long-term implementation.

7.2. HyMPI's PIC + ASIC Engineering Design

Figure 53 shows the functional diagram of the instrument.

Figure 53 : HyMPI functional diagram (Rx: receiver, EOM: electro-optical modulator, SAWG: serial arrayed waveguide grating, BPR: balanced photoreceiver, ASIC: application specific integrated circuit, PD: photodiode).

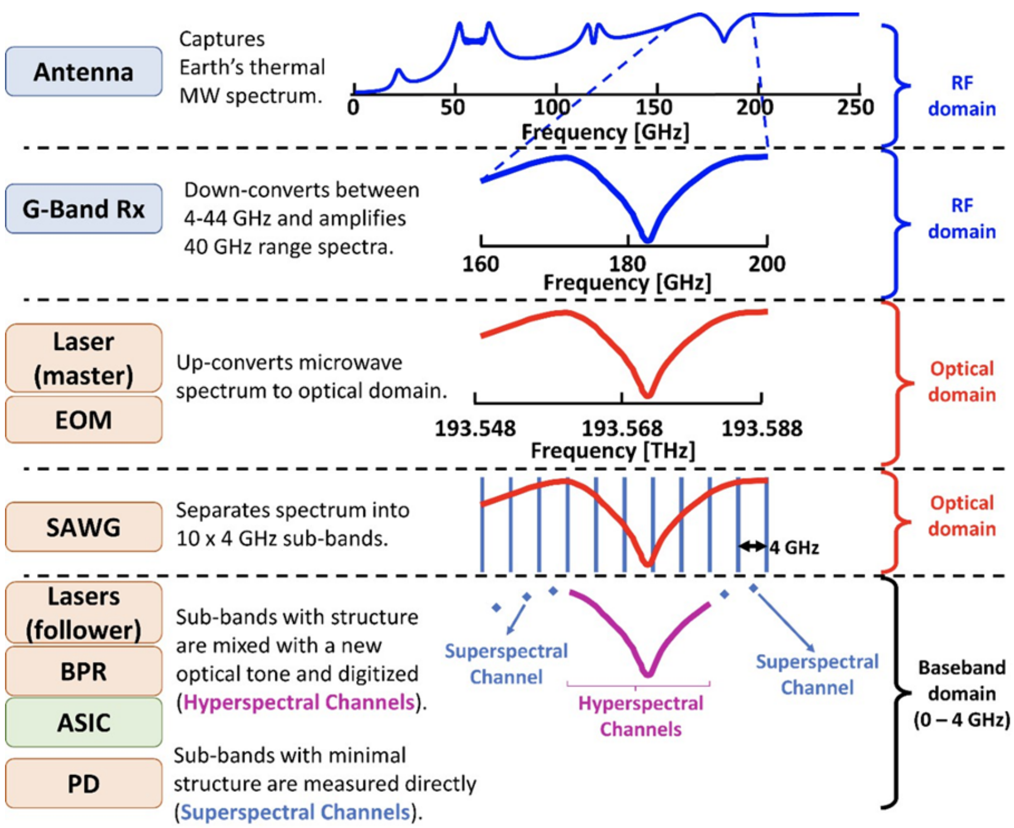

This flowchart illustrates a signal processing chain for microwave spectroscopy, showing the transformation of signals through different frequency domains:

7.2.1. RF Domain (top section)

The antenna captures Earth's thermal microwave spectrum. G-Band Rx: Down-converts frequencies between 4-44 GHz and amplifies signals in the 40 GHz range. HyMPI's implementation covers a 40 GHz bandwidth from 160-200 GHz, modularly designed to be applicable to any region of the 0-200 GHz domain.

7.2.2. Optical Domain (middle section)

An electro-Optical Modulator (EOM) Up-convert the microwave spectrum to the op-tical domain using a laser wavelength of 193.568 THz. The Serial Arrayed Waveguide Grating (SAWG, see section below) separates the spectrum into 10 × 4 GHz sub-bands.

7.2.3. Baseband Domain (0-4 GHz) (bottom section)

A module composed by a laser (follower), BPR, ASIC, and PD Processes the divided signals where sub-bands with structure are mixed with a new optical tone and digitized, labeled as "Hyperspectral Channels" (shown in purple). Sub-bands with minimal structure are measured directly, labeled as "Superspectral Channels" (shown in blue).

The flowchart shows the progression from capturing raw microwave signals from Earth, through frequency conversion and processing stages, ultimately resulting in digitized spectral data that separate signals into hyperspectral and superspectral channels de-pending on their structural characteristics.

The HyMPI program selected the 160-200 GHz region as a case study to demonstrate the PIC + ASIC technology. Importantly, HyMPI technology is frequency-agnostic, and different photonic modules can cover the entire 200 GHz spectrum.

HyMPI has reached TRL 4 and is poised to reach TRL 5 upon completion of upcoming experiments in Earth environmental conditions occurring in the Fall of 2025.

7.3. AURORA Engineering Design

AURORA Pathfinder's engineering design is illustrated in the Figure 54. It is a simplified version of the PIC + ASIC design developed in HyMPI in that it keeps the photonic and ASIC technologies separated. This decision was dictated by the need to test the two technologies independently so as to draw the necessary lessons and reduce risks for AURORA Next Generation. AURORA Next Generation will deploy HyMPI-like PIC+ASIC technology to space. AURORA Next Generation can be a constellation of HyMPI-like modules to achieve full coverage of the Earth's microwave spectrum, realizing the first of its kind sounder + imager sounding architecture in one co-registered and uniform program.

Figure 54: AURORA Pathfinder engineering flow diagram

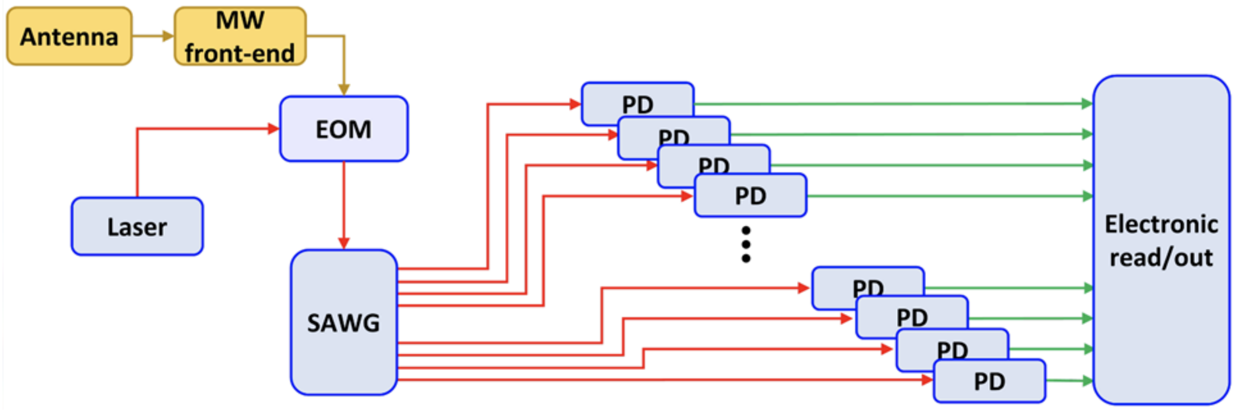

The distinctive element of GSFC MW Photonics technology is the wide-band photonic integrated SAWG, a patented design ([4])) enabling dense and narrow-band channels with high inter-channel crosstalk rejection over a large bandwidth range. The SAWG represents a significant improvement over traditional MW waveguides. It is based on a silicon nitride platform that enables high thermal stability. This translates into high frequency stability of the hyperspectral and superspectral channels and a significant SWAP-C improvement. In Figure 55 a picture of the packaged SAWG is re-ported documenting the dimensions of this module. The packaging provides both electrical interfaces for the waveguide tuning and the optical interfaces for the input/output optical signal. The packaged SAWG is also equipped with a thermo-electric cooler and thermistor that can be used to move the channels to a desired frequency and stabilize the temperature of the PIC.

Figure 55: Picture of the packaged SAWG (left) and microscope picture of the photonic integrated SAWG circuit (right).

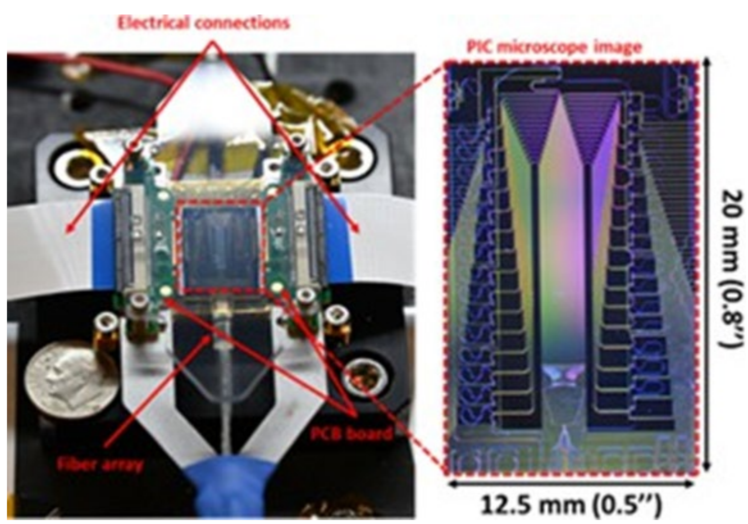

Figure 56 represents the filtering response of the ten channels of the SAWG with about 4 GHz channel separation, 20 dB side-lobe suppression and 2.2 GHz channel bandwidth.

Figure 56: SAWG channels filtering response.

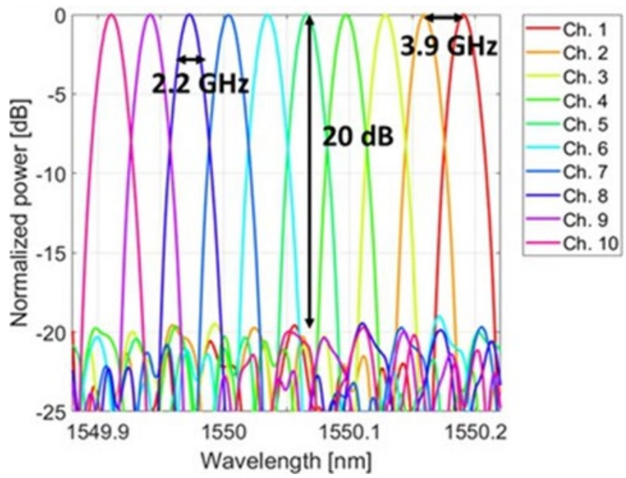

7.4. Measured NEDT

The NEDT of the HyMPI's channels has been evaluated in the laboratory environment. Five simultaneous channels: three superspectral and two hyperspectral resolution channels, were measured to demonstrate parallel sounding capabilities using absorber material and liquid nitrogen for hot and cold targets. the superspectral and hyperspectral channels have been measured with integration times of 16.7 ms and 10 ms, respectively. The number of simultaneous channels was limited by the equipment available in the laboratory. The measurements were performed for simultaneous super- and hyper-spectral resolution channels, for a total of 2051 channels. Figure 57 presents the results for the frequency range between 160 and 200 GHz. The data demonstrates that a single HyMPI module enables simultaneous super- and hyper-spectral resolution channel analysis across a 40 GHz range. The results indicate that the superspectral channels' NEDT is primarily affected by the noise figure of the microwave front-end and transimpedance amplifier gain, while the NEDT of the hyperspectral channels is mostly affected by optical signal strength at the balanced photoreceivers.

Figure 57: HyMPI's superspectral (blue) and hyperspectral (red) NEDT measurement results. In this plot, the superspectral and hyperspectral channels have been measured with integration times of 16.7 ms and 10 ms, respectively. The experimental data have been compared with the predicted NEDT (black

diamonds and lines), obtained by the front-end noise figure, channel bandwidth and integration time.

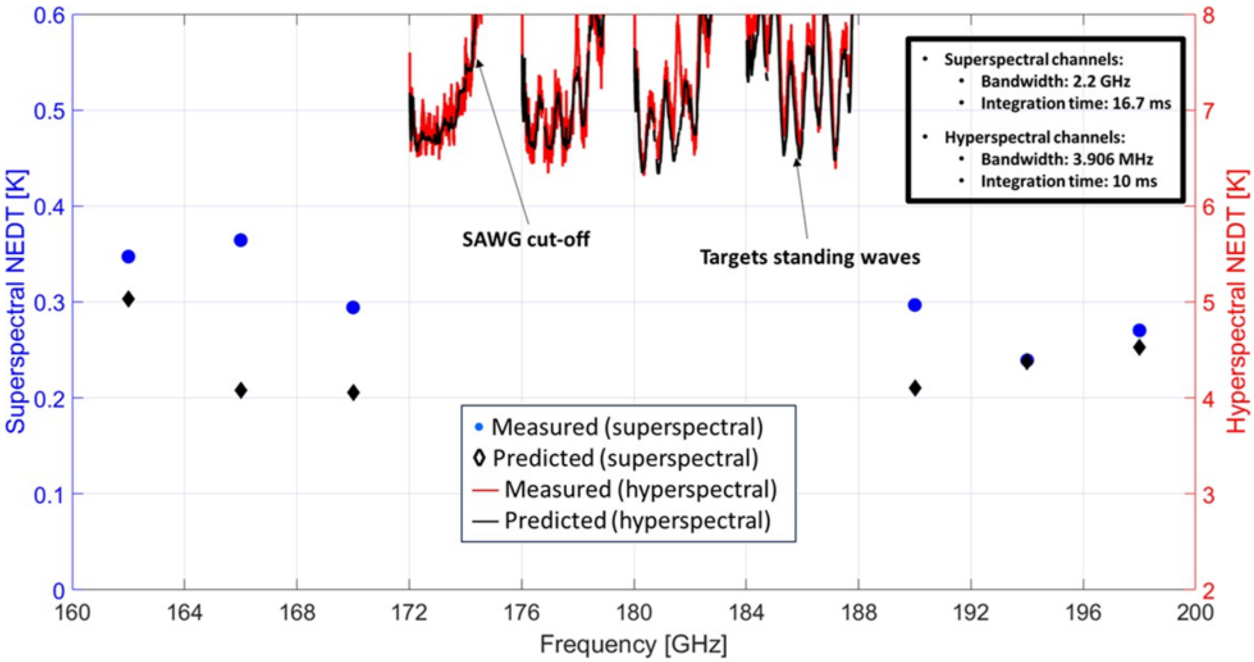

The shape of the hyperspectral NEDT channels is related to the photonic integrated SAWG channel's cut-off bandwidth (see Figure 56), which limits the signal strengths at the balanced photodetectors. This effect will be eliminated in future versions of the instrument by reducing the SAWG optical loss or increasing the SAWG channel bandwidth to 4 GHz. The SAWG filter response is reported in 56. Standing waves are also exhibited in the hyperspectral resolution channels due to the different path lengths between hot and cold targets.

8. Future Work

8.1. CoSMIR-H ongoing improvements and future plans

Critical to instrument performance is addressing the 1/f noise characteristics observed in our Application-Specific Integrated Circuits (ASICs). We are conducting a comprehensive characterization of the 1/f noise patterns identified in the WHyMSIE dataset to establish baseline performance metrics. Concurrently, we are collaborating with PMCC, our ASIC vendor, to optimize device settings and reduce noise levels through targeted parameter adjustments.

Parallel efforts focus on improving our 50-GHz antenna performance. We will conduct detailed antenna measurements to characterize the sidelobes observed in WHyMSIE data. The results of this analysis will likely drive a design iteration to enhance antenna performance for the upcoming NURTURE field campaign (2027), ensuring optimal instrument capabilities for the field campaign. To that end, We are actively preparing the CoSMIR-H instrument for airborne operations, ensuring all systems meet the requirements for integration with NASA’s 777 platform and successful participation in the NURTURE field campaign.

8.2. HyMPI Rooftop Experiment

The NASA-NOAA partnership has made possible the continued development of the Hyperspectral Microwave Photonic Instrument (HyMPI), which is a hyperspectral microwave radiometer capable of processing 5 channels (3 superspectral, 2 hyperspectral) with 4-GHz spectral width simultaneously across a frequency range from 162 - 202 GHz. Unlike traditional radiometers, HyMPI makes use of optical fibers and a novel phototonic integrated circuit (PIC) where incoming signals are upconverted into optical (terahertz) signals as opposed to being managed by traditional microwave wave guides. The data processing table instrument, which include the PIC, laser system, and fiber optic cables along with some sample data from channel 4 (186-190 GHz) can be seen in Figure 58.

Figure 58: HyMPI's tabletop component which includes the photonic integrated circuit and the optical fibers processing incoming data from the feedhorn (left). HyMPI in lab data showing data from channel 4 (186-190 GHz)

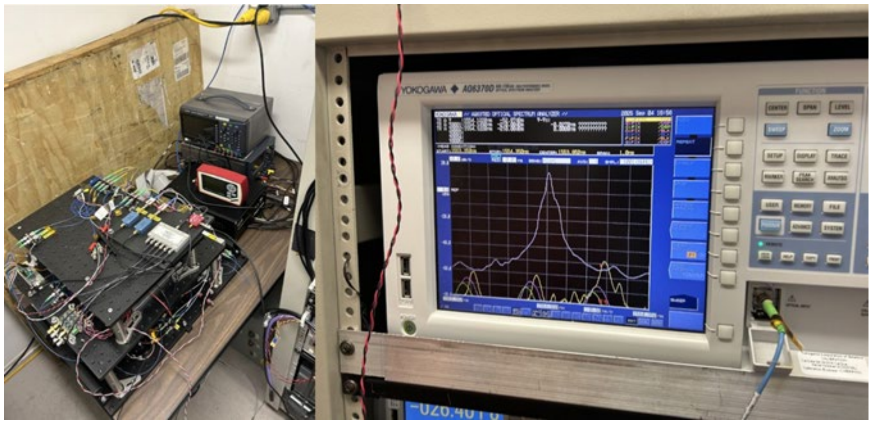

As part of its development, the HyMPI Rooftop Experiment (HRE) will take place on the rooftop of NASA GSFC Building 33 between 09 - 16 September 2025, where HyMPI will be moved out of the lab and will take upward, outdoor radiance measurements. The HRE will be a collaborative effort that will involve the HyMPI development team, Howard University, and the ACHIEVE group. The latter two groups will pro-vide supplementary, but vital ancillary data for HyMPI including radiosonde-based temperature, moisture, and wind profiles, lower-frequency microwave radar data, and W-band radar data, which will be used to characterize the ambient environment and provide information about cloud phase, thickness, and height which will be instrumental for CRTM-simulations of HyMPI data. In addition, building 33 is also home to a sophisticated research-grade weather station that will provide meteorological, ceilometer, all-sky camera imagery that are co-located with HyMPI's sampling location. The HRE will prioritize mid-morning clear sky observations with variable atmospheric water vapor contents and also NOAA-20 and NOAA-21 ATMS afternoon overpasses of opportunity. The channel configuration of HyMPI will include those that align with ATMS channels (i.e., 164 GHz, 183 +/- 7 GHz, 200 GHz) as well as continuous 20 GHz frequency spectra on either side of the 183 GHz atmospheric water vapor channel peak.

8.3. OSSE and deployment of AURORA

Moving forward, we plan to use the grouped channel methodology in upcoming Ob-serving System Simulation Experiments (OSSEs) to evaluate the impact on forecast skill and to assess the practical benefits of hyperspectral microwave observations in a realistic assimilation framework.

Appendix A

A1. Peer Reviewed Journal Publications directly or indirectly supported by this project

Gambacorta, A., Kotsakis, A., Gershman, D., Sharoudi, N., Rosenberg, R., Blaisdell, J., Stegmann, P., D Nicholls, S., Santanello, J., and G Blumberg, W. (2025). , Improved planetary boundary layer sounding using hyperspectral microwave and backscatter LIDAR data fusion. *IEEE, TGRS*. accepted.

Gambini, F., Moreira, R., Robles, D., Gambacorta, A., and Stephen, M. (2024). An Ultra-Compact, Narrow-Bandwidth, and High-Density Channel Photonic integrated channelizer based on serial arrayed waveguide grating architecture. *Journal of Lightwave Technology*, 42(8), 2908–2916. https://doi.org/10.1109/JLT.2024.3349932

Gambacorta, A., et al., (2023). Advancing Atmospheric Thermodynamic Sounding From Space Using Hyperspectral Microwave Measurements. *IEEE Journal of Selected Topics in Applied Earth Observations and Remote Sensing*, 16, 5204–5218. https://doi.org/10.1109/JS-TARS.20233269697.

A2. Conference Proceedings directly or indirectly supported by this project

Kroodsma, Rachael, Ian Adams, Troy Ames, Matthew Fritts, Antonia Gambacorta, Priscilla Mohammed, and Jeffrey Piepmeier. "The Airborne Hyperspectral Microwave Sounder CoSMIR-H." In NASA Decadal Survey Planetary Boundary Layer Incubation Community Meeting. 2025.

Kroodsma, Rachael, Ian Adams, Troy Ames, Matthew Fritts, Antonia Gambacorta, Alexander Kotsakis, Priscilla Mohammed, Stephen Nicholls, and Jeffrey Piepmeier. "Hyperspectral CoSMIR-H Aircraft Instrument and the WH^{2}yMSIE Campaign." In Global Space-based Inter-Calibration System (GSICS) Annual Meeting, 2025.

Gambacorta, Antonia. "The West-coast Heartland Hyperspectral Microwave Sensor Experiment (WH^{2}yMSIE)." In 105th Annual AMS Meeting 2025, vol. 105, p. 451870. 2025.

Shahroudi, Narges, Antonia Gambacorta, John M. Blaisdell, Rachael Kroodsma, Fabrizio Gambini, Jeffrey R. Piepmeier, and Yaping Zhou. "Information Content Analysis of Hyperspectral Microwave Observations in Planetary Boundary Layers" In 105th Annual AMS Meeting 2025

Thomas, Taylor, Shawn Serbin, Alexander Kotsakis, George G. Burba, Antonia Gambacorta, Robert Swap, Edward P. Nowottnick, and Ja-son R. Hupp. "Earth System

Science Across Scales and Organizations: Distributed IoT, Virtual Networks, and integration of Airborne and Spaceborne Remote Sensing." In AGU Fall Meeting Abstracts, vol. 2024, no. 1935, pp. A11S-1935. 2024.

Burba, George G., Taylor Thomas, Shawn Serbin, Alexander Kotsakis, Edward P. Nowottnick, Antonia Gambacorta, and Robert Swap. "NASA WH^{2}yMSIE Airborne Campaign Ground-Truthing: Flux Sta-tions." In AGU Fall Meeting Abstracts, vol. 2024, no. 1943, pp. A11S-1943. 2024.

Serbin, Shawn, Alexander Kotsakis, Antonia Gambacorta, Jeffrey R. Piepmeier, Joseph A. Santanello, Nathaniel W. Chaney, Andrew Feld-man et al. "A multi-scale remote sensing approach to connect land-surface properties and boundary layer dynamics across heterogeneous landscapes." In AGU Fall Meeting Abstracts, vol. 2024, no. 2366, pp. A53R-2366. 2024.

Kotsakis, Alexander, Antonia Gambacorta, Rachael Kroodsma, Ed-ward P. Nowottnick, Matthew McLinden, Shawn Serbin, James P.Mackinnon et al., The West-Coast Heartland Hyperspectral Microwave Sensor Intensive Experiment (WH^{2}yMSIE). In 2024 AGU Fall Meet-ing, vol. 2024, pp. A23Q-07. 2024.

Kroodsma, Rachael, Ian S. Adams, Troy Ames, Matthew Fritts, Antonia Gambacorta, Priscilla Mohammed, and Jeffrey R. Piepmeier. "First Observations from the Airborne Hyperspectral Microwave Sounder CoSMIR-H." In 2024 AGU Fall Meeting, vol. 2024, no. 1937, pp. A11S-1937. 2024.

Shahroudi, Narges, Antonia Gambacorta, John M. Blaisdell, Robert Rosenberg, Rachael Kroodsma, Fabrizio Gambini, Jeffrey R. Piepmeier, Alexander Kotsakis, and Yaping Zhou. "PBL Information Con-tent Sensitivity Study from Passive Measurements: A Case Study from the WH2yMSIE Campaign." In 2024 AGU Fall Meeting, vol. 2024, no. 1949, pp. A11S-1949. 2024.

Stegmann, Patrick, and Antonia Gambacorta. "Evaluation of a Preliminary Forward Operator for the AURORA Hyperspectral Microwave Sounder." In 2024 AGU Fall Meeting, vol. 2024, no. 1949, pp. A11K-1767. 2024.

Stegmann, Patrick, and Antonia Gambacorta. "HyMPI Instrument Trade Study Overview." In NASA Goddard Early Career Scientist Forum, vol. 2024.

Stegmann, Patrick, Narges Shahroudi, Stephen Nicholls, Robert, Rosen-berg, John Blaisdell, and Antonia Gambacorta. "Radiative Trans-fer for Hyperspectral Sounding of the Planetary Boundary Layer." In NASA Decadal Survey Planetary Boundary Layer Incubation Community Meeting, vol. 2025.

Stegmann, Patrick, Narges Shahroudi, Alexander Kotsakis, Stephen Nicholls, Fabrizio Gambini, and Antonia Gambacorta. "Hyperspectral PBL Thermodynamic Structure Observations from Photonic Integrated Circuit Microwave Radiometers." In ESA Living Planet Symposium 2025, vol. 2025, pp. A.01.08. 2025.

Zhou, Daniel K., Hyun-Sung Jang, Allen M. Larar, Xu Liu, Anna M. Noe, Antonia Gambacorta, and Rachael A. Kroodsma. "PBL Thermodynamic Characterization and Its Variability From NAST-I During the WH^{2}yMSIE Field Campaign." In 2024 AGU Fall Meeting. 2024.

Gambacorta, Antonia, Alexander Kotsakis, Rachael Kroodsma, Ed Nowottnick, Shawn Serbin, Amin Nehrir, Matt McLinden et al. "The West-Coast hyperspectral microwave sensor intensive experiment (WHYMSIE)." In IGARSS 2024-2024 IEEE International Geoscience and Re-mote Sensing Symposium, pp. 1430-1432. IEEE, 2024.

Kroodsma, Rachael, Ian Adams, Troy Ames, Matthew Fritts, Antonia Gambacorta, Alexander Kotsakis, Priscilla Mohammed, and Jeffrey Piepmeier. "COSMIR-H: an Airborne Hyperspectral Microwave Sounder for Thermodynamic Sensing of the Planetary Boundary Layer." In IEEE International Geoscience and Remote Sensing Symposium. 2024.

Zhou, Daniel K., Hyun-sung Jang, Xu Liu, Allen M. Larar, Anna M. Noe, Rachael Kroodsma, and Antonia Gambacorta. "Science Applica-tions From NAST-I Measurements: PBL Thermodynamic Characterization and Variation." In EUMETSAT Meteorological Satellite Conference 2024. 2024.

Gambacorta, Antonia, Jeffrey Piepmeier, Joseph Santanello, Mark Stephen, Isaac Moradi, Rachael Kroodsma, John Blaisdell et al. "Advancing Earth's Planetary Boundary Layer Sounding from Space Using Hy-perspectral Microwave Measurements." In IGARSS 2023-2023 IEEE International Geoscience and Remote Sensing Symposium, pp. 1321-1324. IEEE, 2023.

Kotsakis, Alexander, Antonia Gambacorta, James MacKinnon, Jeffrey Piepmeier, Rachael Kroodsma, Joseph Santanello, Greg Blum-berg, John Blaisdell, Isaac Moradi, and Ian Adams. "Hyperspectral Microwave Measurement Demonstrations of Improved Thermodynamic Sounding from Space." In IGARSS 2023-2023 IEEE International Geo-science and Remote Sensing Symposium, pp. 1448-1449. IEEE, 2023.

J. MacKinnon et al., "Deep Neural Networks For Evaluating Future Satellite-Based Hyperspectral Microwave Sensor Designs," IGARSS 2023 - 2023 IEEE International Geoscience and Remote Sensing Symposium, Pasadena, CA, USA, 2023, pp. 5210-5213, doi: 10.1109/IGARSS52108.202

Nicholls, Stephen, Antonia Gambacorta, Rachael Kroodsma, Bob Rosen-berg, John Blaisdell, and Patrick Stegmann. "First Light Results of CoSMIR-H from the WH^{2}yMSIE Field Campaign." In PBL Community Meeting, 2025.

References

[1] A. Gambacorta, A. Kotsakis, and Co-authors. The west-coast hyperspectral microwave sensor intensive experiment (WHyMSIE). IEEE International Geo-science and Remote Sensing Symposium, Athens, Greece, 2024.

[2] A. Gambacorta, J. Piepmeier, M. Stephen, and Co-authors. Advancing atmospheric thermodynamic sounding from space using hyperspectral microwave measurements. IEEE Journal of Selected Topics in Applied Earth Observations and Remote Sensing, 2023.

[3] Antonia Gambacorta, Alexander Kotsakis, Dave Gershman, Narges Shahroudi, Robert Rosenberg, John Blaisdell, Edward Nowottnick, Kenneth Christian, Jordan A. Caraballo-Vega, James MacKinnon, Patrick Stegmann, Stephen D. Nicholls, Joseph Santanello, and William G. Blumberg. Improved planetary boundary layer sounding using hyperspectral microwave and backscatter lidar data fusion. IEEE Transactions Geophs. and Remote Sensing, 2025.

[4] F. Gambini, R. Moreira, D. Robles, A. Gambacorta, and M. Stephen. An ultra-compact, narrow-bandwidth, and high-density channel photonic integrated channelizer based on serial arrayed waveguide grating architecture. Journal of Lightwave Technology, 42(8):2908–2916, 2024.

[5] JCSDA. Crtmv3. https://github.com/JCSDA/CRTMv3, 2025.

[6] B. T. Johnson, C. Dang, P. Stegmann, Q. Liu, I. Moradi, and T. Auligne. The community radiative transfer model (crtm): Community-focused collaborative model development accelerating research to operations. Bulletin of the American Meteorological Society, 104:E1817–E1830, 2023.

[7] I. Moradi. Annual progress report for NASA award number: 80nssc23k0892. Technical report, ESSIC, University of Maryland, College Park, MD, 2025.

[8] P. Stegmann, B. Johnson, I. Moradi, B. Karpowicz, W. McCarty, H. Liu,S. Dutta, and T. Auligne. The community radiative transfer model (crtm): Community-focused collaborative model development accelerating research to operations. The CRTM transmittance coefficient package, 336, 2025.

Acknowledgements

The authors are grateful to the WH²yMSIE Science Team and the NASA Arm-strong Flight Research Center for their participation and support during the field campaign

More information regarding this project

Figure 59: QR Code to access WH²yMSIE Data Archive

This research was supported by NASA ROSES NNH21ZDA001N-DSI, NASA Headquarters, and EUMETSAT research funding.

All WH²yMSIE data are accessible to the public. The WH2yMSIE Data Archive is located at https://www-air.larc.nasa.gov